Lab on a Chip

ROYAL SOCIETY OF CHEMISTRY

CRITICAL REVIEW

View Article Online
View Journal | View Issue

Cite this: *Lab Chip*, 2026, **26**, 1658

Diaphragm-based microfluidic platforms for reconfigurable sample manipulation: from enrichment to activated sorting

Abdullah-Bin Siddique,*[a] Shaghayegh Mirhosseini [a] and Nathan S. Swami *[ab]

Precise manipulation of small sample volumes through enrichment, metering, routing, and selective sorting defines the analytical performance of microfluidic systems. While passive approaches such as deterministic lateral displacement and inertial microfluidics offer robust geometry-encoded separations and field-based techniques like dielectrophoresis, magnetophoresis, and acoustofluidics provide dynamic control, they are limited by inability for tuning, susceptibility to sample media properties, and hardware complexity. Diaphragm-based actuation overcomes these constraints by introducing deformable membranes that dynamically reconfigure channel geometry to achieve sub-second fluidic control without direct exposure to external fields. This review consolidates diaphragm-actuated microfluidic strategies as a unified framework for active sample manipulation, spanning two key functions, enrichment (analyte/cell trapping, ion-transport focusing, and nanoconfinement) and activated sorting (label-based, label-free, and hybrid modalities). Diaphragm materials, geometries, and actuation schemes (pneumatic, piezoelectric, electrostatic, electromagnetic, thermo-pneumatic, and shape-memory) are benchmarked against quantitative performance metrics like pressure–deflection transfer, latency, enrichment efficiency, selectivity, and gating accuracy. Emerging directions include smart fatigue-resistant diaphragm materials, sensor-integrated feedback control, real-time programmable gating, scalable fabrication, and artificial intelligence (AI) to process multimodal data to trigger actuation. By bridging sample enrichment and activated sorting within a single mechanical paradigm, diaphragm-based actuation provides a versatile route towards autonomous, label-free, and high-content lab-on-a-chip systems for next-generation diagnostics, single-cell analytics, and biomanufacturing workflows.

Received 20th October 2025,
Accepted 18th December 2025

DOI: 10.1039/d5lc00984g

rsc.li/loc

1 Introduction

Precise sample manipulation through selective enrichment, routing, metering, and activated sorting of targets from complex matrices is the core enabling function of microfluidic systems. Reliable sample manipulation is essential for translating the gains from microscale transport physics (fast diffusion times, laminar flow streamlines, parallelization, multiplexing and low reagent use) towards integrated systems with improved detection sensitivity and high throughput sorting abilities.[1–3] In practice, the success of lab-on-a-chip assays for clinical, environmental, and bioprocess monitoring hinges on the effectiveness of dynamic enrichment of low-abundance analytes, isolation of rare cells or vesicles, and execution of on-demand gating for selective isolation that is synchronized to upstream detection.[4] Even as chips integrate sophisticated detectors, assay performance continues to depend on sample

Abdullah-Bin Siddique

Abdullah-Bin Siddique is a fourth-year Ph.D. student of Electrical & Computer Engineering at the University of Virginia, conducting his dissertation research on diaphragm-actuated microfluidic systems for biosensing and activated sorting within the Biophysical Microsystems group under the supervision of Prof. Swami. Previously, he completed his MS at the Chonnam National University in Korea completing research on in vitro systems to recapitulate the beating behavior of cardiomyocytes. He is interested in applying his skills in microfabrication to soft nanomaterials, wearable sensing, and tissue and lab-on-a-chip systems.

[a] *Electrical & Computer Engineering, University of Virginia, Charlottesville, VA, 22904 USA. E-mail: gcx2vm@virginia.edu, nswami@virginia.edu*
[b] *Chemistry, University of Virginia, Charlottesville, VA, 22904 USA*

manipulation for reproducible control of picoliter to nanoliter volumes,[5] formation and release plugs on cue,[6] and enrichment of rare targets without fouling or carryover.[7–9] These demands require devices capable of rapid and tunable reconfiguration of microscale geometries, particularly when handling heterogeneous biological samples with wide ranging physical properties (size, shape, morphology, deformability).

Current sample manipulation strategies are broadly classified into passive and active modes. Passive methods, such as deterministic lateral displacement (DLD)[10] arrays and inertial fluidics[11] offer geometry-encoded separations that are robust, scaled to high throughputs, and require minimal external hardware. However, since their property thresholds are fixed by device geometry during fabrication, these methods have limited capacity to accommodate variable sample properties such as viscosity, hematocrit, or particle deformability, and cannot often provide the rapid gating or dynamic confinement needed for time-sensitive analytical workflows.[12–16] Active methods including dielectrophoresis (DEP), magnetophoresis, and acoustofluidics are dynamic due to tunable force fields and enable label-free selectivity, yet their performance is strongly dependent on buffer composition, electrode stability, and impedance-matching, which constrain operation under biologically relevant conditions.[17–24] These limitations become restrictive for biological targets with wide distributions in size, morphology, viability, and mechanical stiffness including single cells, cellular aggregates, extracellular vesicles, and subcellular scale bioparticles. Fixed device geometries or field conditions often struggle to maintain selectivity and throughput under such variability, underscoring the need for actuation strategies capable of mechanically reconfiguring channel dimensions and flow trajectories on demand.

Diaphragm-based actuation strategies address these gaps by using a deformable membrane for on-demand reconfiguring of the channel geometry and for pump-free direction of fluid flow. A diaphragm can open/close/pinch channels with sub-second latency,[25] meter volumes and generate pump-free flow,[26,27] while locally creating tunable nano-constrictions that serve as perm-selective elements for ion-transport focusing.[28] Flow parameters can also be synchronously controlled with optical/electrical detection, while reducing sample exposure to electrodes or strong flow fields.[29,30] While pneumatic PDMS membranes established the foundation for reliable valving/pumping and large-scale microfluidic integration, newer actuation schemes, such as electrostatic, electromagnetic, and thermo-pneumatic fields reduce external infrastructure and enable portable systems.[31–34] Hence, diaphragm geometries provide a mechanical framework for integrating these actuation schemes towards implementing tunable confinement, selective enrichment, and rapid gating across diverse sample types and analytical tasks.

While diaphragm systems historically developed in microfluidics in the form of multilayer valves and pumps patterned on elastomers for transistor-like large-scale valve integration[35] and picoliter metering that is agnostic to fluid properties,[36] they have recently emerged as a system of programmable transducers that detect local conditions to create on-demand reconfiguration of channel geometry. Classic so-called "Quake-valves" operate at modest pressures with reliable sealing and milliseconds scale actuation and have been densely integrated for high-throughput biochemical workflows.[37,38] Subsequent generations introduced lifting-gate geometries to minimize dead volume and leakage during sample injection, using materials that extend beyond PDMS to include parylene-C and glass to enhance chemical compatibility, pressure tolerance, and dimensional stability.[39–43] Parallel progress in

Shaghayegh Mirhosseini

Shaghayegh Mirhosseini is a second-year Ph.D. student of Electrical & Computer Engineering at the University of Virginia, conducting her dissertation research on biophysical cytometry and biosensing systems within the Biophysical Microsystems group under the supervision of Prof. Swami. Previously, she completed her MS at the University of Tehran, Iran, completing research on optofluidic integration with microfluidic separation. She is interested in applying her skills in microfabrication and image processing to microfluidic separation, single-cell cytometry and biosensing.

Nathan Swami

Nathan Swami serves as Professor of Electrical & Computer Engineering at the University of Virginia, with joint appointments in the Chemistry department and the Cancer Center. His research group develops heterogeneously integrated microsystems that couple biofabricated microenvironments with in-line microfluidic detection, control, and data analytics for phenotype-selective information to advance their clinical translation. His recent honors include the 2021 Mid-Career Award from the AES Electrophoresis Society and the Interdisciplinary Research Award from the VP, Research Office at University of Virginia in 2022. He seeks to impact diagnostic systems within point-of-care and resource-poor settings for advancing precision medicine.

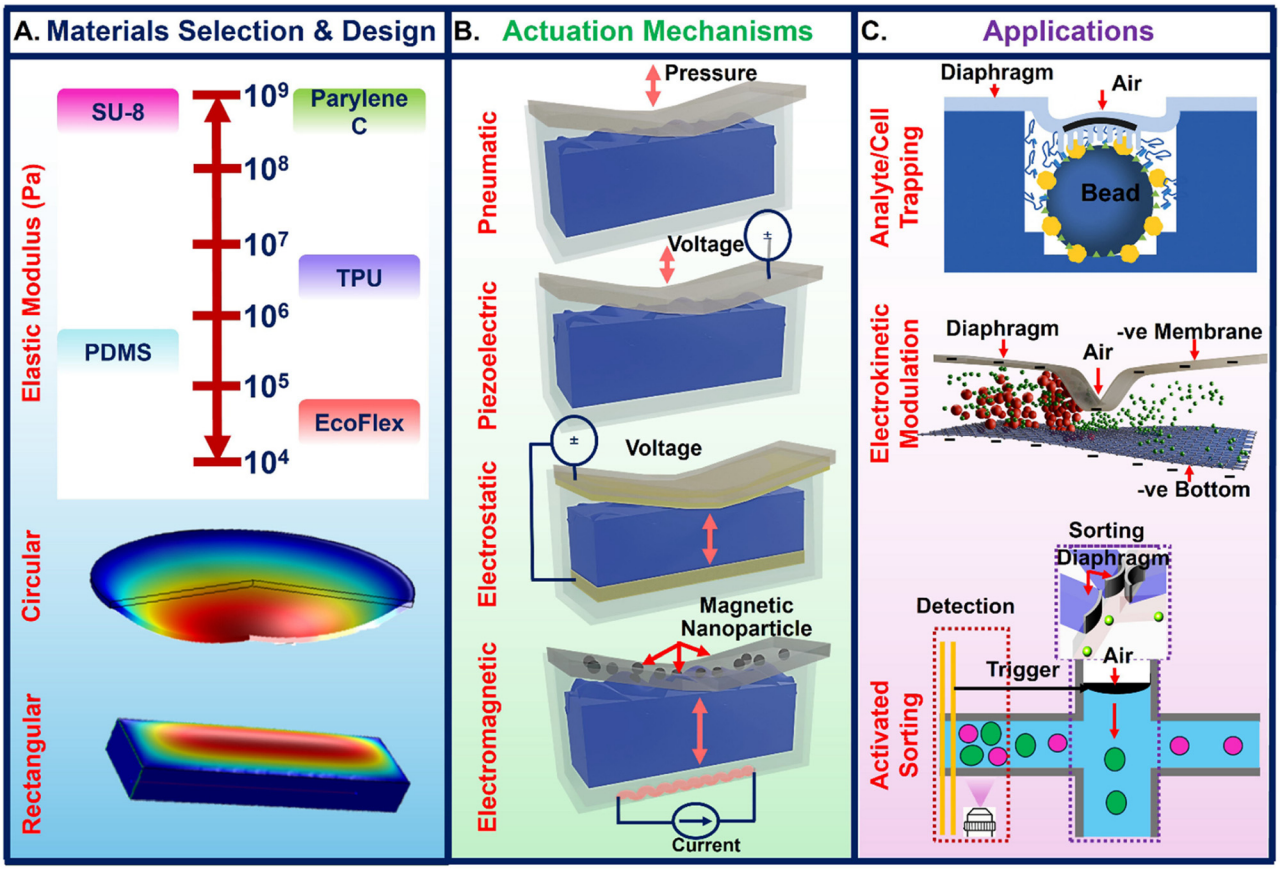

Fig. 1 Schematic of diaphragm architectures and actuation strategies employed in microfluidic platforms, highlighting their roles in sample enrichment and activated sorting applications.

electrostatic and thermochemical actuation has demonstrated low-power and compact control (including normally closed devices and millisecond membrane strokes) that can be driven by portable electronics, thereby reducing their reliance on bench-top pneumatics.[32,44,45] These advances are reframing diaphragms from simple on/off flow elements to active sample-manipulation transducers.

Based on this context and drawing upon recent reviews on passive separations (DLD,[13,46] inertial[47,48]), field-based actuation (DEP,[49] acoustofluidics,[50,51] magnetofluidics[20]), and microvalve engineering;[52,53] this review organizes diaphragm-based systems according to the underlying mechanical and materials design principles (Fig. 1A) that govern their actuation mechanisms (Fig. 1B) for application to sample enrichment and activated sorting (Fig. 1C). Our novel contribution is the critical analysis of the performance of diaphragm microsystems based on interplay of their materials design and mechanical response (section 2) with operational metrics for actuation (Tables 1 and 2), thereby linking these factors to their application for sample enrichment and activated sorting (section 3) through comparison of key performance metrics (Tables 3 and 4). Through highlighting emerging directions (section 4), such as smart diaphragm materials, sensor-integrated feedback control, real-time gating, and artificial intelligence (AI) to process multimodal data to trigger actuation, this review connects materials design to mechanical response and to programmable transducer integration for application of diaphragm systems towards sample enrichment and sorting within lab-on-a-chip

Table 1 Influence of diaphragm geometry on actuation

Diaphragm shape	Boundary condition	Maximum deflection formula	Key parameters	Ref.
Circular (radius a)	All edges clamped	$w_{max} = \frac{3(1-\nu^2)}{16Eh^3}\Delta P a^4$	E-Young's modulus, ν-Poisson's ratio, h-diaphragm thickness, ΔP-pressure, a-radius	81
Square (length a)	All edges clamped	$w_{max} = \frac{\Delta P a^4}{47D}, D = \frac{Eh^3}{12(1-\nu^2)}$	Same as above	82
Rectangular (length a × width b)	All edges clamped	$w_{max} = \alpha(\nu, a/b)\frac{\Delta P a^4}{Eh^3}$	α-shape factor, aspect ratio a/b	83

Table 2 Various diaphragm actuation mechanisms, listed with their design parametric equation and their performance metrics

Actuation mechanism	Parametric equation	Key parameters	Displacement	Response time	Advantages	Limitations	Ref.
Pneumatic	$w = \frac{3(1-\nu^2)}{16Eh^3}\Delta P a^4$	w-Displacement, E-Young's modulus, ν-Poisson's ratio, h-diaphragm thickness, ΔP-pressure, a-radius	>100 μm	<50 ms	Large stroke, simple fabrication	Bulky pressure source, limited miniaturization	70
Piezoelectric	$\Delta L = d_{33} \times V$	ΔL-Change in length, d_{33}-piezoelectric coefficient, V-applied voltage	<50 μm	<1 ms	Fast, precise, MHz operation	Limited stroke, high voltage, brittle ceramics	86, 87
Electrostatic	$F = \frac{1}{2}\varepsilon_0 A\frac{V^2}{d^2}$	F-Electrostatic force, ε_0-vacuum permittivity, A-area, V-voltage, d-gap distance	<10 μm	<1 ms	Low power, MEMS-compatible	Small force, dielectric breakdown, pull-in instability	90
Electromagnetic	$F = I\cdot(L \times B)$	F-Lorentz force, I-current, L-wire length vector, B-magnetic field	<50 μm	10–100 ms	Programmable force, non-contact	Joule heating, fabrication complexity	91
Thermo-pneumatic	$P = \frac{nRT}{V}\ \Delta P \propto \Delta T$	P-Pressure, T-temperature, n-gas moles, R-gas constant, V- volume	<100 μm	>1 s	Simple, low-cost	Slow, energy inefficient	93
SMA/SMP	$\varepsilon = \frac{\Delta L}{L_o}$	ε-Strain, ΔL-change in length, L_0-original length	<200 μm	0.5–5 s	High actuation force, reversible, programmable	Slow, fatigue, thermal load	94, 95

platforms for molecular diagnostics, single-cell analytics, and biomanufacturing workflows.

2 Diaphragm materials design for actuation

This section is focused on diaphragm materials design considerations that influence their mechanical response and the selection of device geometries for realizing various actuation mechanisms.

2.1 Diaphragm material selection

The material properties of diaphragms dictate their mechanical response, actuation dynamics, chemical compatibility, and operational lifetime within microfluidic platforms. Poly-dimethyl-siloxane (PDMS) is the most used substrate material, due to its excellent elastomeric properties that present a tunable Young's modulus ranging from ~0.5 MPa to 3 MPa (Fig. 2A), depending on crosslinking ratio and curing conditions.[54,55] While the optical transparency and biocompatibility of PDMS are also of interest, its drawbacks include high gas permeability, solvent-induced swelling, and mechanical fatigue under cyclic actuation. These factors are detrimental for long-term applications (>10^5 cycles) involving actuation at high frequencies (>50 Hz) or high-pressures (>100 PSI).[56]

To address the limitations of PDMS, composite materials have been extensively explored. Carbon nanotube (CNT)-reinforced PDMS, especially with ~1–5 wt% multi-wall CNT loading (Fig. 2B), has demonstrated >50% enhancement in tensile strength and in greater durability under cyclic actuation, without significantly compromising their elastic or optical properties.[57–60] For applications requiring ultra-soft diaphragms and large stroke deflection, Ecoflex™ offers low Young's modulus values (~0.05–0.2 MPa) and >600% elongation at break (Fig. 2C), although these occur at the expense of geometric stability and enhanced hysteresis arising from long-term mechanical memory.[61–63] On the other end of the stiffness spectrum, SU-8 and parylene-C are used to fabricate thin, high-frequency resonant diaphragms with elastic moduli in the GPa range, enabling nanometer-scale precision actuation under electrostatic or piezoelectric fields, albeit with minimal stroke amplitude and poor fatigue behavior.[64,65] Emerging classes of stimuli-responsive hydrogels and shape memory polymers (SMPs) are also being incorporated as smart diaphragms, though challenges, such as cycle-to-cycle drift, higher response times, encapsulation, solvent compatibility, and delamination limit their ability to achieve consistent and reversible actuation in microfluidic formats.[66,67] Ultimately, material selection must be closely aligned with the actuation modality, desired stroke amplitude, chemical resistance, target analyte compatibility, and intended device longevity for each application.

2.2 Diaphragm geometry selection

The design geometry of a diaphragm governs its deformation characteristics under an applied force, as well as its resonant behavior, stress distribution, and fluidic displacement capabilities. In microfluidic membranes, "geometry" encompasses not only shape and thickness, but also how the diaphragm is supported or constrained, since these boundary conditions directly determine the achievable deflection and uniformity of deformation (Table 1). The shape of the diaphragm, typically circular, square, or rectangular, directly influences the uniformity of deflection and the maximum sustainable stress. Circular diaphragms are generally preferred due to their inherent symmetry and the absence of sharp corners, which distributes stress levels evenly and provides predictable, axisymmetric deflection profiles.[68,69]

Table 3 Various diaphragm actuated enrichment platforms and their performance metrics

Actuation mechanism	Material/ composite	Diaphragm shape	Actuated displacement	Actuation frequency	Application	Enrichment	Ref.
Pneumatic *via* solenoid valve	PDMS	Rectangular	N/A	100 ms	Peptide enrichment (leucine enkephalin, angiotensin II, GGYR)	450-fold (leucine enkephalin) 100-fold (peptide mix)	102
Pneumatic *via* solenoid valve	PDMS	Circular	N/A	350–3500 ms	DNA enrichment (λ-DNA in water, TE buffer, cell lysate, lysed blood)	>53% of total DNA	103
Pneumatic	PDMS	Rectangular	~15 μm	Static	Enzymatic enrichment (ELF-97/ALP, HRP/tyramide reaction)	2.4-fold enzymatic reaction rate 2.8-fold single-molecule reaction	106
Pneumatic	PDMS	Rectangular	~15 μm	Static	Enrichment of Ewing sarcoma EV biomarkers for digital immunoassay (CD99, NGFR, EZR, ENO-2)	>300-fold in limit of detection compared to ELISA	107
Pneumatic *via* solenoid valve	PDMS	Circular	~600 μm	0.1–10 Hz	Aptamer enrichment and screening (HT3-R9R/thrombin binding)	~20-fold at 10 nM DNA ~4-fold at 100 nM DNA	108
Pneumatic	PDMS	Rectangular	N/A	200 ms	Single-cell trapping and intracellular Ca^{2+} monitoring (NIH-3T3 and HeLa cells)	Enhanced Heterogenous cell response to chemical stimulation	110
Pneumatic	PDMS	Rectangular	25 μm	Static	Single cells capture and isolation (Jurkat cells)	Parallel isolation of 60 cells	111
Pneumatic (compressed air/mineral oil)	PDMS	Circular	50 μm	Long term static (3 hours)	Jurkat cells and PBMCs enzymatic assay (granzyme B protein)	~4000 Jurkat cells assayed ~2800 PBMC assayed	112
Pneumatic	PDMS	Rectangular	44 μm	Static/dynamic	Mechanically activated artificial cell creation	N/A	113
Pneumatic	PDMS	Rectangular	N/A	Static	High-throughput integrated single-cell RT-qPCR (K562 cells)	1000-Fold reduction in reagent consumption	37
Pneumatic	PDMS	Rectangular	N/A	Static	Single-cell mRNA isolation, cDNA synthesis, qPCR analysis (NIH/3T3 cells)	80% efficient mRNA isolation	115
Pneumatic *via* solenoid valve	PDMS	Rectangular	~13.5 μm	Static	Electrokinetic concentration polarization	1000-Fold (fluorescein)	119
Pneumatic *via* syringe pumps	PDMS	Semicircular	~8 μm	Static	Enrichment of biomolecules (*E. coli*, avidin, and biotin-coated microparticles)	10-Fold local fluorescence intensity increase	120
Pneumatic *via* pressurized DI water	PDMS	Rectangular	~50 μm	Static	Alexa Fluor 488 enrichment *via* ion concentration polarization (ICP)	Enhanced local analyte concentration	28
Piezoelectric (indirect bending)	Stainless steel	Circular	60 μm	30 Hz	Lukemia cell enrichment (K-562)	87.1% intact cells	104
	Silicon	Rectangular	10–20 μm	350 Hz		64% intact cells	
Piezoelectric (steel pressing pin)	Fused silica	Circular	~100 nm	Static (gradual)	Enrichment for ELISA (cytokine IL-6)	1500 IL-6 molecules (25 pL sample)	105

Diaphragm thickness plays a critical role in balancing mechanical stiffness with actuation sensitivity. Typical PDMS diaphragms used in sorting devices range from 10–50 μm in thickness, achieving deflections >50 μm under pressure <10 kPa.[70] Thinner diaphragms enhance compliance but are more susceptible to rupture, while thicker ones require higher actuation force and may dampen dynamic response. Geometric compliance can also be tuned through pre-stretching or pre-stress, which modifies the diaphragm's baseline curvature and effective stiffness, thereby shifting its deformation response and natural frequency.[71,72] Similarly, boundary conditions such as clamped, hinged, or partially supported edges are geometric constraints that define the deflection shape, energy distribution, and pressure–deflection relationship. Fully clamped diaphragms tend to exhibit the most predictable and repeatable deformation behaviour, whereas partially supported designs can be engineered for large-stroke, low-energy actuation or bistable operation.[73–76] As these geometric factors interact nonlinearly in elastomeric membranes, finite element analysis (FEA) simulations are commonly used as a tool to optimize the diaphragm shape, thickness, pre-stress, and boundary constraints by predicting deflection profiles and stress distributions under different actuation conditions.[77–80]

2.3 Diaphragm actuation mechanisms

The actuation mechanism determines how energy is transferred into diaphragm deformation and its ultimate translation towards pump-free fluid displacement or flow gating. Each

Table 4 Various diaphragm based activated sorting platforms and their performance metrics

Actuation mechanism	Material/composite	Diaphragm response Time	Detection mechanism	Detection throughput	Sorting type	Application	Sorting Performance	Ref.
Piezoelectric	PZT bonded to stainless steel	0.1–1 ms	Fluorescence detection using PMT + spatial filter	~500 particles per s	Labeled	Cell per particle sorting (fluorescence beads)	Sorting rate 330 particles per s Sorting efficiency ~70% Sorting error 0%	121
Piezoelectric (pull–push relay mode)	2 integrated PZT disk	0.8 ms	Confocal fluorescence+ forward scattering + PMTs	1100–2500 cells per s	Labeled	Mammalian cell sorting (HeLa cells)	Sorting rate ~1250 cells per s Sorting efficiency ~98% Selectivity ~89%	122
Piezoelectric (external actuator)	Borosilicate glass	16 μs	Fluorescence detection using PMT	N/A	Labeled	Cell sorting (*E. gracilis* and GCIY)	For *E. gracilis*: sorting rate 23 kHz Sorting efficiency 92.8% Selectivity 95.8% For GCIY cells: Sorting rate 11 kHz Sorting efficiency 97.8% Selectivity 98.9%	123
Piezoelectric	Piezoelectric ceramic disc bonded to stainless steel	~2.2 ms	Confocal epifluorescence using PMT	75–150 cells per s	Labeled	Cell sorting (*E. coli*)	Sorting Efficiency 44%	124
Laser induced cavitation bubble	N/A	30 μs	Fluorescence detection using PMT	1500-20000 cells per s	Labeled	Mammalian cell sorting (Nalm-6 and Ramos)	Selectivity ~38–90%	127
Laser induced cavitation bubble	N/A	20 μs	Fluorescence detection using PMT	~45 000 cells per s	Labeled	Mammalian cell sorting (Ramos human Burkitt)	Sorting efficiency 97% Selectivity ~45–96%	128
Piezoelectric (external actuator)	PDMS	>1 ms	Fluorescence detection using a multi-pixel photon counter (MPPC)	100 000 cells per s	Labeled	Cell sorting (MCF-7)	Sorting rate 6400 cells per s Selectivity ~82%	125
Piezoelectric (external actuator)	Flexible membrane	<1 ms	Fluorescence based cytometry	12 000 cells per s (24 parallel channels)	Labeled	Cell sorting (T cells)	Sorting efficiency 80% Selectivity ~97%	126
Piezoelectric (bimorph actuator)	PZT ceramic	~5.8 ms	Bright field + fluorescence imaging using PMT	100 cells per s	Labeled	Cell sorting (HEK-293T, MDCK, human glioblastoma cells)	Selectivity ~92%	132
Piezoelectric (external actuator)	PDMS	0.383 ms	Fluorescence based detection using hi speed camera + CNN (ResNet18) classification	~2000 particles per s	Labeled	Particle sorting	Sorting rate 22.1 particles per s Sorting efficiency 95% Selectivity ~99.4%	133
Pneumatic *via* solenoid valve	PDMS	~4 ms	Fluorescence detection using PMT	2000 particles per s	Labeled	Aqueous droplet sorting	Sorting rate 250 Hz Sorting efficiency 99.99%	129
Pneumatic *via* solenoid valve	PDMS	~50 ms	Optical transmission based transmitted light intensity (TLI)	20 droplets per s	Labeled	Water-in-oil droplet sorting	Sorting rate 20 droplets per s Sorting efficiency 100%	130
Pneumatic *via* solenoid valve	PDMS	~7.4 ms	Epifluorescence based detection using PMT	50 Hz	Labeled	Droplet per cell sorting (droplets, ACHN)	Sorting rate 50 droplets per s Sorting efficiency (droplets 98% ACHN cells 83%) Selectivity (droplets 98.9%	131

Table 4 *(continued)*

Actuation mechanism	Material/composite	Diaphragm response Time	Detection mechanism	Detection throughput	Sorting type	Application	Sorting Performance	Ref.
							ACHN cells 87-90%)	
Piezoelectric (2 external actuator)	PDMS	~1 ms	Dual frequency impedance detection	~50 000 cells per s	Label free	Cell sorting (Jurkat and MDA-MB-231)	Sorting rate 1000 cells per s Selectivity 95%	134
Piezoelectric	PZT bonded to PDMS	N/A	Multi frequency impedance cytometry	50 particles per s	Label free	Microcarrier per cell aggregate sorting (Cytodex-3, alginate microparticles, 3D cells aggregates/spheroids)	Sorting rate ~5–10 particles per s Selectivity ~80%	135
Pneumatic *via* solenoid valve	PDMS	50 ms	Microscopic image processing using a *k*-nearest neighbor (*k*NN) algorithm	0.2 cells per s	Label	Cell sorting (budding yeast cells)	Selectivity ~97%	136
Pneumatic using DSP microcontroller	N/A	~15 ms	Brightfield image-based deep learning classification using a CNN (InceptionV3)	12 000 events per s	Label free	Rare cell sorting (NSCLC, HCC, fetal nucleated RBCs, DTCs)	Sorting rate 6000 cells per min Sorting efficiency 50% Selectivity 33%	137
Piezoelectric	Piezoelectric ceramic	<3 ms	Brightfield image acquisition using PMT	~600 events per s	Label free	Human leukocytes sorting (granulocytes, lymphocytes, monocytes)	Sorting rate ~200 cells per s Selectivity (lymphocytes 92.0%, monocytes 89.05%, granulocytes 98.4%)	138
Pneumatic *via* capillary tuned solenoid valve system	N/A	~1.7 ms	hotoacoustic detection using transmission mode photoacoustic microscopy	~66.8 cells per min	Label free	Cell sorting (*Haematococcus pluvialis*)	Sorting rate ~0.77 Hz	139
Piezoelectric	PZT bonded to cyclo olefin copolymer (COC)	N/A	Transmission imaging using a scanning Bessel Gaussian laser beam and PMT	~300 cells per s	Label free	Cell sorting (SKNO1 leukemia cells, and *Scenedesmus* green algae)	Sorting rate ~300 cells per s Selectivity (leukemia cells 97%, Scenedesmus 98%)	140
Piezoelectric (2 external pull–push actuator)	Dual glass membrane	1.1 ms	FT-CARS Raman spectroscopic imaging + support vector machine (SVM) classification	50 cells per s	Label free	Mammalian cell sorting (3T3-L1, hiPSCs, *Chlamydomonas* sp., *Euglena gracilis*)	Sorting rate 50 cells per s Sorting efficiency 94% Selectivity 97%	141
Piezoelectric	Metal bimorph piezoelectric disc bonded to PDMS	0.5 ms 10 ms	Electrical size based detection *via* resistive pulse sensing (RPS) Fluorescence based optical detection using CCD	~100 000 particles per s 100 particles per s	Label free Labeled	Particle per cell sorting (beads, fluorescent beads, Hoechst stained murine macrophage)	Sorting rate ~1000 particles per s Sorting efficiency 98% Selectivity 98% Sorting rate ~100 particles per s Sorting efficiency 95% Selectivity 94.5%	87
Piezoelectric (2 external pull–push actuator)	Dual glass membrane	0.5 ms	Bright-field imaging + CNN classifier Fluorescence based detection using PMT	100 cells per s	Label free Labeled	Rare cell sorting (HL60, RBCs, MCF-7, WBCs, miPS-CART, MEF feeder cells)	Sorting efficiency (HL60 90.6%, MCF-7 88.2%) Selectivity (HL60 96.3%, MCF-7 95%) Sorting efficiency (miPS-CART 87%) Selectivity (miPS-CART 93.8%)	142

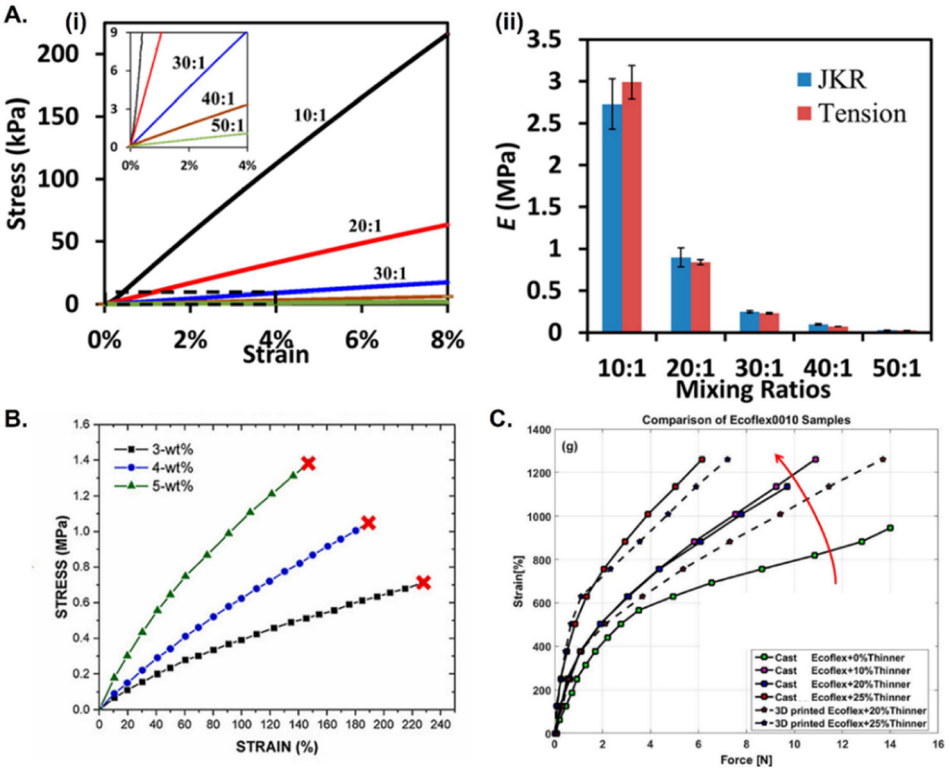

Fig. 2 Mechanical properties of common diaphragm materials. A. Stress–strain response of PDMS with different base-to-curing ratios (inset shows higher range of ratios) (i) tension tests reveal the influence of mixing ratio on elasticity, and (ii) Young's modulus values determined by Johnson–Kendall–Roberts (JKR, blue) and tensile testing (red) highlight method-dependent variations.[55] Reproduced from ref. 55 with permission from Springer Nature, © 2015. B. Stress–strain curves of PDMS/MWCNT composites at varying filler loadings, illustrating reinforcement effects.[59] Reproduced from ref. 59 with permission from Elsevier, © 2024. C. Strain-force behavior of Ecoflex 0010 with different thinners to demonstrate the tunable compliance.[62] Reproduced from ref. 62 with permission from Elsevier, © 2020.

actuation modality imposes specific constraints on device integration, responsiveness, amplitude, and energy consumption. Pneumatic actuation is the most widely employed method, particularly in multilayer PDMS platforms with microvalves and peristaltic pumps. Diaphragms deflect under external pressure (typically 5–30 kPa), controlled *via* solenoid valves or pressure regulators, to achieve displacements of >100 μm within 50 ms.[41,84,85] Positive pressure deforms the diaphragm downward and vacuum or negative pressure lifts it upward (Fig. 3A). The simplicity of fabrication and large force output make pneumatic systems ideal for sample manipulation and channel gating, although they require bulky off-chip infrastructure and are limited by pressure delivery latency and tubing dead volume. Beyond pneumatic systems, several electrically driven actuation modalities provide faster response times and more compact integration. Piezoelectric actuation often utilizes bonded PZT discs or cantilevers to the diaphragm to expand or contract upon voltage application, causing diaphragm deflection (Fig. 3B). The deflection is rapid but is typically small in amplitude. This method provides sub-millisecond response time with high-frequency excitation (up to MHz) and is well-suited for sorting based on high-speed triggering (*e.g.*, from fluorescence detection), particle focusing, or droplet generation.[86–88] Electrostatic actuation uses attraction forces between a conductive diaphragm and a fixed electrode upon voltage application. Voltage pulls the diaphragm downward, reducing the air gap (Fig. 3C). Though energy-efficient and compatible with monolithic integration, electrostatic forces scale poorly with gap size and require extensive cleanroom processing steps and fine control of dielectric isolation layers.[89,90] In electromagnetic actuation, a diaphragm embedded with a magnetic material is actuated by the Lorentz force generated from current flowing through an embedded microcoil (Fig. 3D). These systems offer programmable force control *via* current modulation, with stroke amplitudes of sub 100 μm and frequency response in the ~10–200 Hz range.[91] However, this method is limited by Joule heating, complexity in coil fabrication, and magnetic shielding for high-sensitivity applications. Several thermal and material-responsive strategies offer alternatives to electrically driven mechanisms to deform diaphragms, albeit with slower response times. Thermo-pneumatic actuation leverages thermal expansion of trapped air or phase-change materials to induce diaphragm deflection (Fig. 3E). Although simple and low-cost, thermal systems are inherently slow (>1 s response), energy-inefficient, and susceptible to thermal crosstalk.[92,93] A less-known actuation mechanism is based on shape memory alloys (SMAs) and shape memory polymers (SMPs) that deform upon heating and return to their original shape upon cooling or *via* chemical/environmental triggers (Fig. 3F). These offer reversible

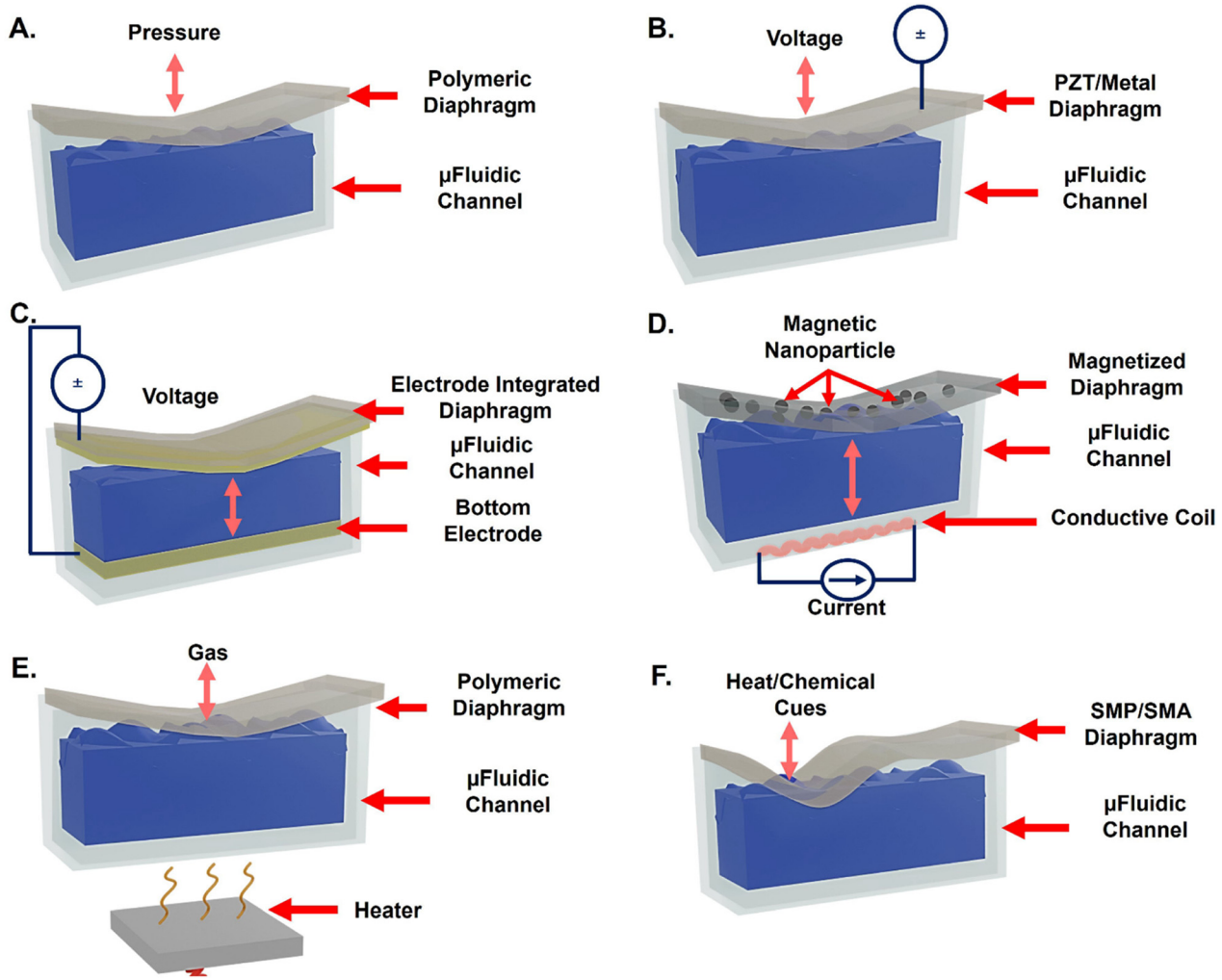

Fig. 3 Actuation mechanisms of diaphragm based microfluidic platforms. A. Pneumatic actuation. B. Piezoelectric actuation. C. Electrostatic actuation. D. Electromagnetic actuation. E. Thermo-pneumatic actuation. F. Shape memory alloy/polymer actuation.

chemical or thermal responsiveness, but with long cycle times and limited force output.[94,95] Recent trends include hybrid actuation strategies combining pneumatic priming with piezo or electrostatic fine control, thereby enabling fast, tuneable, and large-range actuation that is tailored to the demands of enrichment and sorting. Overall, the performance of diaphragm-based microfluidic platforms is governed by the interplay between material properties, geometric constraints, and actuation modality. Material selection defines the elastic range, fatigue resistance, and chemical compatibility of the membrane, while geometric parameters including shape, thickness, and boundary constraints dictate the deformation profile and achievable stroke. Per Table 2, actuation mechanisms further determine response speed, force output, operational stability, and system-level integration. Together, these factors establish the practical limits on pressure-deflection behavior, latency, and long-term reliability. Despite substantial progress, current diaphragm systems face challenges related to mechanical drift under continuous cycling, variability in large-area deformation, and trade-offs between stroke amplitude and actuation bandwidth. Future work will benefit from the development of hybrid material stacks with improved fatigue resistance, geometry-tailored membranes that decouple stiffness from stroke, and multimodal actuation schemes that combine coarse and fine control. Integrating real-time sensing or feedback mechanisms into diaphragm elements also represents a promising direction for enabling adaptive, self-correcting microfluidic architectures.

3 Diaphragm actuated sample manipulation

3.1 Evolution of diaphragm-based microfluidic actuators

Diaphragm-based elements have progressively transitioned from simple on/off microvalves to programmable modules capable of actively manipulating samples at micro- and nanofluidic scales. This design evolution provides the architectural foundation for their enrichment (section 3.2) and activated sorting (section 3.3) strategies. Early diaphragm platforms primarily functioned as robust flow-control units.

Actuated by pneumatic or electrostatic mechanisms, these membranes provided reversible deformation for valve sealing, peristaltic pumping, and localized trapping, while minimizing electrical interference with sensitive biological samples. Initial adoption was limited by fabrication complexity and control-hardware requirements, but advances in multilayer soft-lithographic bonding, compliant membrane patterning, and high-speed pneumatic or piezoelectric control systems improved responsiveness, reliability, and ease of integration. Early demonstrations by Satoh *et al.*[96] showed pneumatically actuated corrugated diaphragms that produced tight sealing with minimal dead volume, maintained pressure drops below ~100 Pa at 10 sccm, and operated leak-free up to ~150 kPa. Perdigones *et al.*[97] advanced this concept by introducing an NMOS-like "fluidic transistor" in which diaphragm deflection modulated flow with gain (a small variation in control pressure generating disproportionately large changes in output flow). This architecture improved operational efficiency by reducing the control pressure required for reliable switching while enabling fine analog modulation across a broad dynamic range. The next stage of development shifted from single-element valves to densely addressable networks. Quake-style multilayer soft-lithography enabled monolithic integration of normally open and normally closed valves formed by orthogonally bonded control and flow layers in PDMS, supporting picoliter-scale routing, metering, and isolation with minimal dead volume.[98] Diaphragm valves and pumps have also been applied to implement frequency-encoded flow programming capable of executing multi-step microfluidic workflows.[99] These fluidic logic architectures provided the first truly programmable microfluidic environments and directly updated later diaphragm-driven enrichment and sorting workflows. Subsequent adaptations, such as lifting-gate designs, introduced a geometric inversion, wherein a flexible diaphragm lifts away from a rigid seat to open the channel, rather than collapsing downward into it. This simplifies its integration with plastic substrates and provides flexible assembly formats by employing a common actuation base with interchangeable disposable cartridges for automated immunoassays, while maintaining high efficiency.[26] Hybrid diaphragm implementations expand the accessible mechanical and chemical design space. Electrostatic microvalves integrating parylene-C diaphragms with PDMS flow layers combined robust sealing with lower actuation thresholds, with design parameters refined using finite-element simulations to minimize pull-in voltage and maintain stable cycling.[33] At smaller length scales, glass-based based nanofluidic platforms employing elastically deformable nanochannel diaphragms demonstrate precise valve switching and stable control over gas–liquid interfaces, sustaining more than 10^5 actuation cycles at MPa-level pressures over $>10^5$ cycles.[100] This illustrates that diaphragm valves can retain mechanical integrity and reproducibility, even under extreme pressure drops of nanofluidic operating conditions. These developments collectively positioned diaphragms as versatile transducers for micro- and nanofluidic sample manipulation. Pneumatically actuated PDMS diaphragms with lateral dimensions of ~1–1.5 mm support μL min^{-1} flow rates and >100 μm stroke within tens of milliseconds, enabling precise gating, plug formation, and pump-free routing.[101] Continued geometric miniaturization and chamber optimization has further enabled sub-300 nL volume control with sub-second response times, supporting high-resolution metering and nanofluidic enrichment workflows.[34] Together, these advances establish diaphragms as actively tuneable actuators capable of dynamically modulating confinement, pressure, and flow pathways; functions that underpin modern micro- and nanofluidic enrichment and selective particle manipulation.

3.2 Application to sample enrichment

Diaphragm actuation has transformed microfluidic enrichment strategies by enabling dynamic confinement, selective trapping, and controlled release of analytes and cells. Unlike static microstructures or purely passive capture methods, diaphragm-based systems provide programmable and reversible control over local microenvironments, thereby allowing precise regulation of binding, washing, and elution steps. In this subsection, we detail how these advances have been implemented for analyte/cell trapping, nanoconfinement-based enrichment, and electrokinetic modulation.

3.2.1 Analyte trapping and analysis. Diaphragm-actuated trapping enables dynamic, geometry-based confinement of affinity elements, allowing analytes to be immobilized, incubated, and released within precisely defined microenvironments. By deforming a membrane to localize functionalized beads or surfaces within a capture zone, the diaphragm establishes a reversible affinity matrix that enhances reaction kinetics, controls analyte residence time, and supports repeated regeneration of the capture interface. This approach provides tunable mechanical control that is difficult to achieve using static posts or chemically patterned traps. In these systems, diaphragm deflection is used to repeatedly position or compress beads/surfaces against localized regions of the flow, enabling selective binding under continuous perfusion followed by controlled washing and release. Cong *et al.*[102] developed a pneumatic microvalve that functioned as an electrokinetic pre-concentrator and hydrodynamic injector. Valve closure produced nanoscale gaps that supported concentration polarization, enabling ~450× peptide enrichment within 230 s, while reopening directed the pre-concentrated plug downstream with pressure-driven flow and minimal dilution. This illustrates how diaphragm-generated gaps can couple analyte enrichment and dye injection within a single structure. Building on this concept, programmable valve sequencing has been leveraged to automate bead loading, washing, incubation, and elution across multi-step assays.[103] These automation strategies have been further diversified through hybrid actuation schemes that integrate diaphragm motion with electrical, acoustic, or sensor-triggered cues and it further expands control over timing and shear exposure during enrichment workflows.

Bußmann *et al.*[104] investigated piezoelectric micro diaphragm pumps for gentle transport of viable cells in microfluidic systems to analyze how different actuation waveforms affect shear-induced damage, flow efficiency, and pump performance during label-free cell handling in complex media. As a result, diaphragm motion not only controls spatial confinement but also governs hydrodynamic stresses that influence assay integrity. Precise analyte isolation at very small volumes has been enabled through piezo-actuated nanovalves that deform thin glass membranes to form sub-100 nm channels on demand, as demonstrated by Sano *et al.*,[105] who achieved trapping of ~1500 IL-6 molecules in picoliter volumes and performed single-cell-level ELISA (enzyme-linked immunosorbent assay) within an integrated nanofluidic platform (Fig. 4B). This shows how diaphragm-like actuation can be extended to rigid materials to achieve high-fidelity trapping in the picoliter regime. Further advances have focused on improving spatial resolution and microenvironment tuning. Micropost-reinforced PDMS diaphragms create 3D nanoconfined reaction zones that enhance analyte retention and increase enzyme-substrate contact by mechanically modulating the accessible volume under ~40 kPa actuation pressurest.[106] Similar nanoconfinement topographies were adapted to improve extracellular vesicle capture *via* affinity enhancement (Fig. 4C).[107] More recent architectures, such as the micro-to-nano ($\mu 2n$) multi-well platform, integrate liquid-metal strain sensors directly into diaphragms to enable real-time feedback on deflection and nanoconfinement state.[108] This allowed precise well-to-well control of confinement depth and flow sequencing to support high-throughput enrichment and molecular screening (Fig. 4D).

Despite these advantages, diaphragm-based analyte trapping faces several constraints. Sequential valve actuation limits throughput, especially when multiple capture zones need to be independently cycled, and nanogap-based enrichment can vary with small deviations in deformation or bead alignment. Integrating beads or nanostructures within compliant membranes may also pose fouling risks and require careful geometric registration. Even so, the ability to regenerate capture zones, modulate confinement in real time, and couple mechanical trapping with sensor feedback provides a level of adaptability that static microstructures cannot achieve. These attributes position diaphragm-actuated enrichment as a route toward robust, multiplexable, and high-content molecular assays.

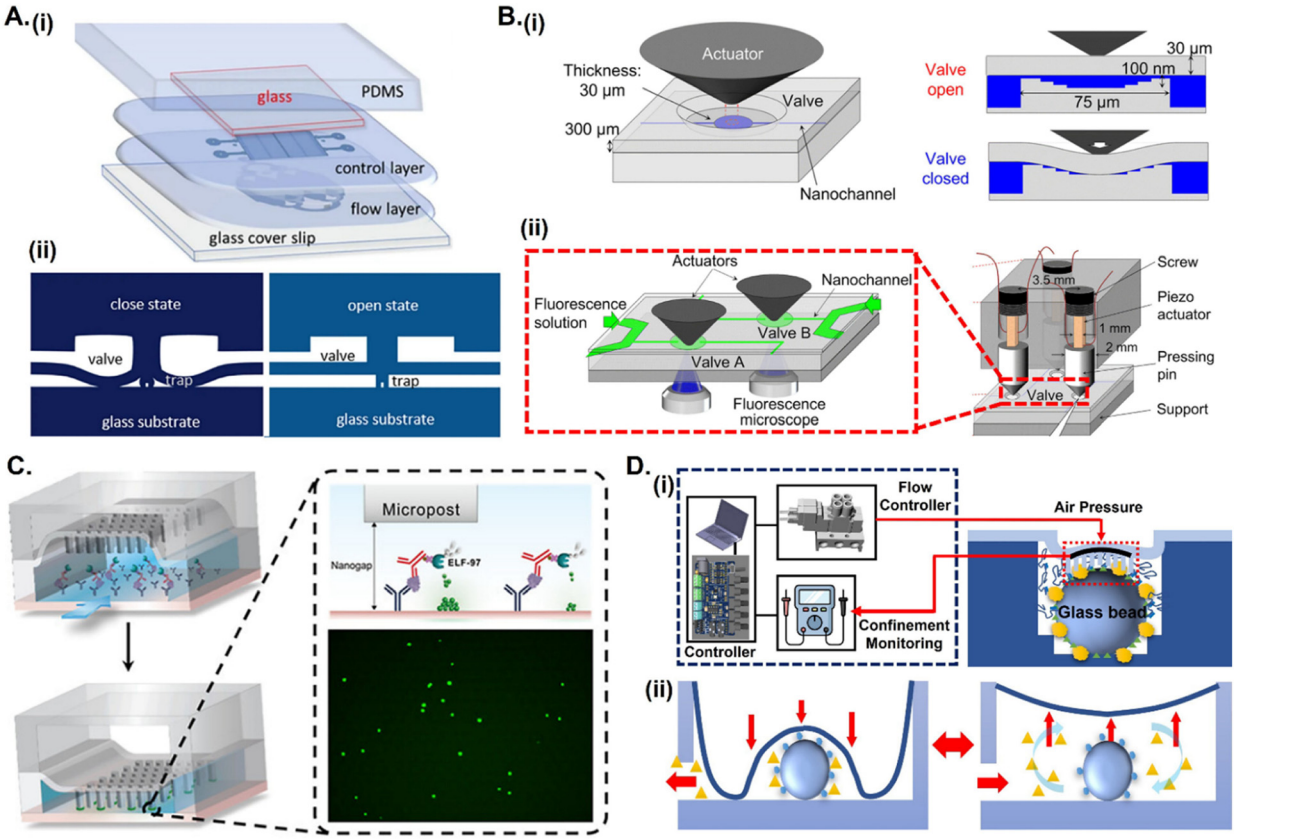

Fig. 4 Diaphragm-enabled analyte enrichment platforms. A. (i) A multilayer microfluidic device for simple cell trapping, and (ii) its pneumatic diaphragm driven capture mechanism.[112] Reproduced from ref. 112 with permission from Springer Nature, © 2021. B. (i) Schematic illustration of a nanogap based system for biomolecule confinement, and (ii) illustration of the integrated actuation and detection module.[105] Reproduced from ref. 105 with permission from the Royal Society of Chemistry, © 2023 C. Partition-free digital immunoassay facilitated by micropost arrays in combination with polymeric diaphragm actuation.[107] Reproduced from ref. 107 with permission from the American Chemical Society, © 2025. D. (i) Schematic of an automated nanoconfinement system for DNA enrichment, demonstrating diaphragm mediated switching between nanoconfined trapping and bulk transport modes (ii).[108]

3.2.2 Single cell trapping and analysis. Diaphragm-based actuation enables precise, reversible mechanical confinement of individual cells to support dynamic immobilization, selective stimulation, and downstream molecular profiling within well-controlled microenvironments. By integrating deformable PDMS membranes with programmable valve timing, these platforms overcome the stochastic capture behavior of hydrodynamic traps and the limited isolation fidelity of microwells, thereby allowing single cells to be positioned, stimulated, and released with high temporal precision. Foundational work on microchamber-based systems using elastomeric diaphragm valves have shown that mechanically defined compartments can isolate single cells in tightly regulated femto- to nanoliter reaction volumes for controlled capture, stimulation, and lysis.[109] Wang *et al.*[110] introduced a pneumatically switchable trap in which rapid diaphragm deflection selectively immobilized suspended cells, permitted localized chemical stimulation, and then released each cell on demand, to enable interrogation of intracellular calcium dynamics. Pressure pulses as short as 200 ms produced activation responses equivalent to longer exposures, while rapid buffer exchange supported cellular recovery for return to baseline calcium levels within ~30 s, demonstrating robust functional interrogation under reversible confinement. Hsiao *et al.*[111] combined positive dielectrophoretic capture with diaphragm-actuated nanoliter compartments, using microfabricated electrodes for precise cell positioning and membrane deflection to isolate and lyse individual cells for on-chip molecular assays. To increase parallelization, Briones *et al.*[112] fabricated an array of ~5000 hydrodynamic traps, each sealed by a circular diaphragm valve optimized through simulations to reduce the sealing pressure to ~0.07 MPa. This configuration enabled thousands of single-cell enzymatic assays in parallel and resolved heterogeneity in granzyme B activity across Jurkat and PBMC populations (Fig. 4A). Beyond natural cells, Ho *et al.*[113] engineered diaphragm-controlled compression and aspiration of double emulsion "artificial cells," wherein modulation of the oil layer thickness induced calcium influx, establishing a mechanosensitive synthetic cell model. Diaphragm platforms have also been integrated with single-cell gene expression workflows, wherein microvalve-based systems coordinate capture, lysis, reverse transcription, and qPCR (real time polymerase chain reaction) within nanoliter volumes. White *et al.*[37] and Sanchez-Freire *et al.*[114] demonstrated parallel processing of hundreds of single cells, thereby reducing reagent use and measurement noise by confining all assay steps within a tightly regulated chamber. Marcus *et al.*[115] further applied diaphragm-assisted isolation to mRNA purification and cDNA synthesis, enabling detection of low-abundance transcripts from individual cells.

Despite these advances, scalability remains limited by the need to actuate thousands of valves in parallel, and leakage or incomplete sealing under long-term confinement constrains stability, particularly for assays requiring extended incubation. Ensuring uniform valve performance across large arrays is a critical design challenge that microwell systems do not face. Even so, diaphragm-actuated single-cell systems offer deterministic capture, reversible confinement, and seamless coupling to downstream biochemical or mechanical assays, providing a level of control and information content that surpasses purely hydrodynamic or microwell-based approaches. Their ability to integrate functional stimulation, transcriptional readouts, and mechanobiological perturbation within the same physical architecture positions diaphragm actuation as a powerful route toward high-content single-cell analysis.

3.2.3 Ion concentration polarization and electrokinetic modulation. While nanoslits[116,117] fabricated through conventional lithography provide fixed geometries for generating localized ion concentration polarization (ICP),[118] diaphragm-actuated nanochannels offer a mechanically tunable alternative that reduces fabrication complexity and enables dynamic control of permselectivity, gap height, and hydrodynamic coupling. Unlike static nanoslits, wherein the fluidic geometry and perm-selective interface are permanently defined, diaphragm deflection creates nanoscale gaps on demand, allowing pressure-driven flow to be coupled with localized electric-field gradients, in ways that static structures cannot readily support. This tunability improves enrichment sensitivity, focusing stability, and operational flexibility. Quist *et al.*[119] demonstrated that elastomeric microvalves can function as reconfigurable nanochannels, wherein pressure-induced diaphragm deformation forms perm-selective nanogaps that support multiple ICP regimes (Fig. 5A). By coordinating valve actuation with applied voltages, the deformable gap established anodic counter-gradient focusing (ACGF), producing ~1000-fold preconcentration of charged analytes such as fluorescein within ~100 s, followed by controlled plug release upon membrane reopening. This coupling of mechanical gating with electrokinetic focusing illustrates how diaphragm-generated nanogaps directly modulate both ion transport and analyte flow. Sabbagh *et al.*[120] similarly used pneumatically actuated microvalves to deform elastomeric membranes into tuneable nanochannels that transition into ion-permselective states. Dynamic gap modulation allowed stable depletion zones and concentration-polarized layers to form under continuous flow, thereby enabling field-induced focusing and ~10-fold enrichment of fluorescent dyes and biomolecules. Because the nanochannel height could be varied in real time, the platform maintained focusing performance across different flow rates and buffer conditions, which is not achievable with rigid nanoslits. Building on these principles, pneumatically actuated PDMS micro-diaphragm valves have been used to modulate ion transport across Nafion-coated microchannels.[28] Here, diaphragm deflection adjusts the effective contact area and local electric field distribution at the Nafion interface, permitting on-demand formation, translation, or dissipation of ICP layers. This enables spatially controlled preconcentration plugs whose position and intensity can be tuned without altering the underlying membrane chemistry (Fig. 5B). The significance of this approach lies in decoupling the ion-exchange membrane

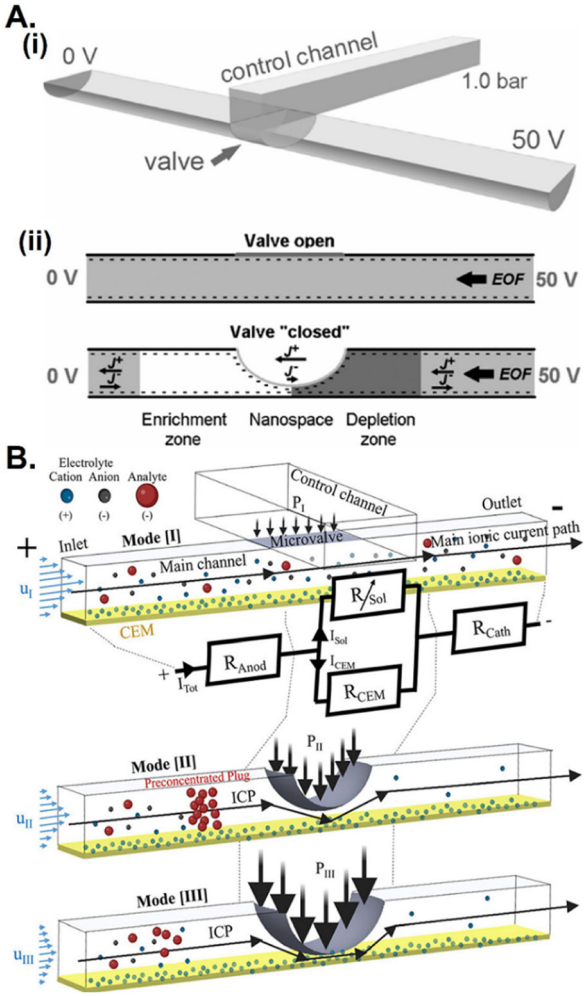

Fig. 5 Diaphragm-actuated control of ion concentration polarization and enrichment. A. (i) Microvalve schematic and (ii) the onset of concentration polarization under applied voltage and pressure.[119] Reproduced from ref. 119 with permission from the Royal Society of Chemistry, © 2013. B. Pressure regulated transport modes: Ohmic conduction (I), ICP with analyte enrichment (II), and ICP with negligible plug formation (III). The diaphragm valve defines the overlap of main and control channels, while the cation exchange membrane mediates selective ion transport.[28] Reproduced from ref. 28 under a CC-BY 4.0 license.

from fixed channel geometry, thereby allowing active gating of ICP zones that remain static in conventional devices. Despite these capabilities, diaphragm-driven ICP performance is shaped by several constraints. A fundamental trade-off exists between gap size and permselectivity: smaller gaps enhance ion selectivity but increase hydrodynamic resistance, while larger gaps reduce enrichment efficiency. Depletion zones may destabilize during valve transitions, leading to variability in plug formation, and the focusing regime is buffer-dependent, shifting with ionic strength and pH. Furthermore, unlike static nanoslits whose geometry is constant, diaphragm-generated nanogaps require precise pressure control to maintain reproducibility, particularly under multistep actuation sequences. Recent strategies have improved robustness while preserving tunability. Coupling diaphragm-formed gaps with fixed ion-exchange membranes enhances permselectivity, while retaining mechanical control. FEM-guided optimization of actuation set-points enables more reproducible nanogap formation. Sequenced valve timing, where pressure and voltage transitions are staged to avoid collapse or overexpansion of depletion zones, has been shown to stabilize polarization layers and improve plug consistency. Together, these developments underscore how mechanically reconfigurable nanogaps extend ICP control beyond what static nanoslits can achieve, enabling enriched, precisely positioned analyte plugs for downstream biochemical analysis.

To conclude section 3.2, these diaphragm-actuated strategies demonstrate how mechanical reconfigurability can control analyte trapping, single-cell interrogation, and nanoscale electrokinetic enrichment within a single device framework (Table 3). By using diaphragm motion to modulate confinement, transport, and local field gradients, these platforms offer a level of spatial and temporal precision that static microstructures cannot provide. Nonetheless, common constraints including valve leakage, variability in nanogap formation, buffer-dependent polarization behavior, and challenges in scaling to thousands of parallel units continue to limit throughput and reproducibility. Continued integration of real-time sensing, feedback-controlled actuation, and hybrid architectures that couple diaphragm deformation with ion-selective materials or dielectrophoretic interfaces will be essential for improving robustness. Overall, the tunability and regeneration capacity of diaphragm-actuated systems position them as a versatile foundation for high-content biochemical analysis, bridging microscale reaction control with single-cell and nanoscale enrichment capabilities.

3.3 Activated sorting

Diaphragm-actuated sorting systems represent a transformative class of microfluidic platforms that use elastomeric or piezoelectric membranes to selectively manipulate cells and particles in response to signals from upstream detection events. These systems offer rapid, reversible, and biocompatible actuation that is ideal for high-throughput cytometry, particularly as workflows evolve toward more integrated, automated, and application-specific diagnostics. These systems can be classified into distinct categories based on detection techniques: label-based, label free, and hybrid, as discussed below.

3.3.1 Marker dependant label-based sorting. Marker-dependent label-based sorting leverages externally applied fluorescent, genetic, or antibody-based reporters to identify target cells or droplets, while diaphragm actuation provides the mechanical impulse required for rapid and selective flow switching. By decoupling molecular recognition (*via* labeling) from physical displacement (*via* diaphragm motion), these systems achieve high specificity in situations wherein the unlabeled populations would otherwise overlap in size, deformability, or electrical phenotype. Diaphragm-based

platforms therefore rely on a two-step mechanism, optical or biochemical identification followed by pressure-, piezo-, or cavitation-induced deflection, which enables precise routing even in compact or disposable chip formats. Piezo-driven diaphragm actuation forms one of the most established approaches for marker-dependent sorting, owing to its sub-millisecond mechanical response and compatibility with high-speed fluorescence detection. Chen *et al.*[121] introduced a compact microchip sorter in which piezoelectrically driven diaphragm oscillation (~1.7 kHz) generated high-frequency lateral flow perturbations (Fig. 6A), thereby enabling fluorescently labeled *E. coli* to be sorted at 330 cells s^{-1} with sub-milliwatt power consumption and waveform-programmable control. Cheng *et al.*[122] extended this strategy by integrating piezo bending actuators directly onto a disposable microfluidic chip (Fig. 6B), achieving enrichment of mammalian cells from 3.36% purity to >90% purity with a five-log enrichment factor under sterile, aerosol-free operation. Diaphragm placement and jet geometry also influence performance for larger or adherent cells, as demonstrated by Sakuma *et al.*,[123] who positioned dual piezo-driven diaphragms externally along a wide channel (Fig. 6C) to stabilize high-speed local flows and sort large cells without compromising throughput. Zhao *et al.*[124] applied a diaphragm-based FACS system to perform directed evolution of fluorescent calcium indicator variants (Y-GECO), pre-screening ~10^6 mutants at ~300 cells s^{-1} (Fig. 6D). Cai *et al.*[125] further demonstrated the versatility of piezo-driven sorting by developing a closed-loop μ-CFACS platform that used fast amplified piezoelectrically actuated on-chip valves (OPVs) for rapid flow-switching, paired with pneumatic cylinder actuated valves (OCVs) for recirculating and enriching rare fluorescently labeled cells across multiple cycles, thereby enhancing recovery and purity, while eliminating contamination risk. Hulspas *et al.*[126] extended piezo-actuated sorting into GMP environments by using an externally driven piezoelectric pin coupled to a diaphragm to isolate fluorescenctly-tagged regulatory T cells while maintaining sterility and viability. Collectively, these platforms highlight how piezo-mediated deflection offers a tuneable balance between actuation speed, displacement amplitude, and chip-level footprint for fluorescence-triggered sorting.

Laser-induced cavitation represents a second major class of diaphragm-like actuation, in which explosive vapor bubble formation substitutes for mechanical membrane deformation to achieve ultrafast jetting. Wu *et al.*[127] developed a pulsed-laser activated sorter (PLACS) wherein explosive vapor bubbles deflected fluorescently labeled mammalian cells within ~30 μs, achieving 20 000 cells per s throughput with >90% viability and high-purity operation, using only ~90 pL of fluid displacement. Chen *et al.*[128] further optimized this by implementing 3D hydrodynamic focusing to confine the bubble jet perturbation and reduce off-target dispersion, to enable a throughput of 23 000–45 000 cells per s with >90% purity in high-purity mode and 45% in enrichment mode, all within a single-stage, single-channel platform. These cavitation-based devices demonstrate that optical triggers paired with micro-jet deflection can reach kHz-scale sorting rates, far exceeding the mechanical response limits of conventional pneumatic valves.

Marker-dependent droplet sorting constitutes another important branch, wherein each droplet serves as an isolated reaction vessel whose fluorescence determines its routing. Abate *et al.*[129] integrated a high-speed pneumatic valve at an asymmetric bifurcation, allowing laser-triggered actuation to sort droplets at up to 250 Hz with <3 ms valve response times and error rates below 0.01%, while avoiding dielectric constraints inherent to electrostatic droplet sorters. Building on this, Chen *et al.*[130] designed a bilayer pneumatic valve configuration that flanked an inclined sorting region, enabling three-way droplet routing based on absorbance-derived optical signals (Fig. 6F). Although broadly compatible, throughput remained limited (~20 Hz) due to slower valve recovery. Jin *et al.*[131] later refined this architecture using a passive flow-aligner and optimized valve geometry (Fig. 6G), which stabilized droplet trajectories and reduced false-positive errors by fivefold, while enlarged valve cross-sections decreased actuation time by a factor of three. These refinements enabled >98% accuracy sustained at 50 Hz across emulsions, cell suspensions, and hydrogel droplets. Together, these devices illustrate how diaphragm-controlled pneumatic gating provides gentle, material-agnostic manipulation that is especially valuable for optically encoded droplet assays. Recent systems increasingly integrate real-time computational analysis with diaphragm actuation to enable context-aware sorting decisions. Gu *et al.*[132] combined on-chip imaging with deep-learning classification to assess both fluorescence intensity and morphological features, to allow diaphragm-triggered routing with enhanced specificity (Fig. 6E). Similarly, Lee *et al.*[133] developed a CNN-guided sorter capable of executing label-based decisions within 50 ms per cycle, thereby yielding a compact system suitable for decentralized diagnostic workflows. These intelligent platforms highlight how diaphragm-mediated flow switching can be tightly coupled to software-defined decision layers to enable a richer database for sorting than offered traditionally by solely based on fluorescence magnitude. Despite these technological advances, marker-dependent sorting faces persistent challenges, including photobleaching, phototoxicity, the need for exogenous labels, and throughput ceilings that remain below those of commercial FACS instruments. Cavitation-based approaches achieve tens of kHz, but pneumatic and piezo-mechanical systems remain limited by millisecond-scale membrane response times. Even so, diaphragm-based platforms offer buffer-independent operation, gentle hydrodynamic conditions, sealed architectures for sterile handling, and seamless integration with machine-learning-driven decision logic. Emerging recirculating μ-CFACS systems and AI-triggered sorters demonstrate the potential of diaphragm-actuated architectures to complement conventional FACS by delivering compact, contamination-resistant, and selectively programmable cytometry for sample preparation and diagnostics.

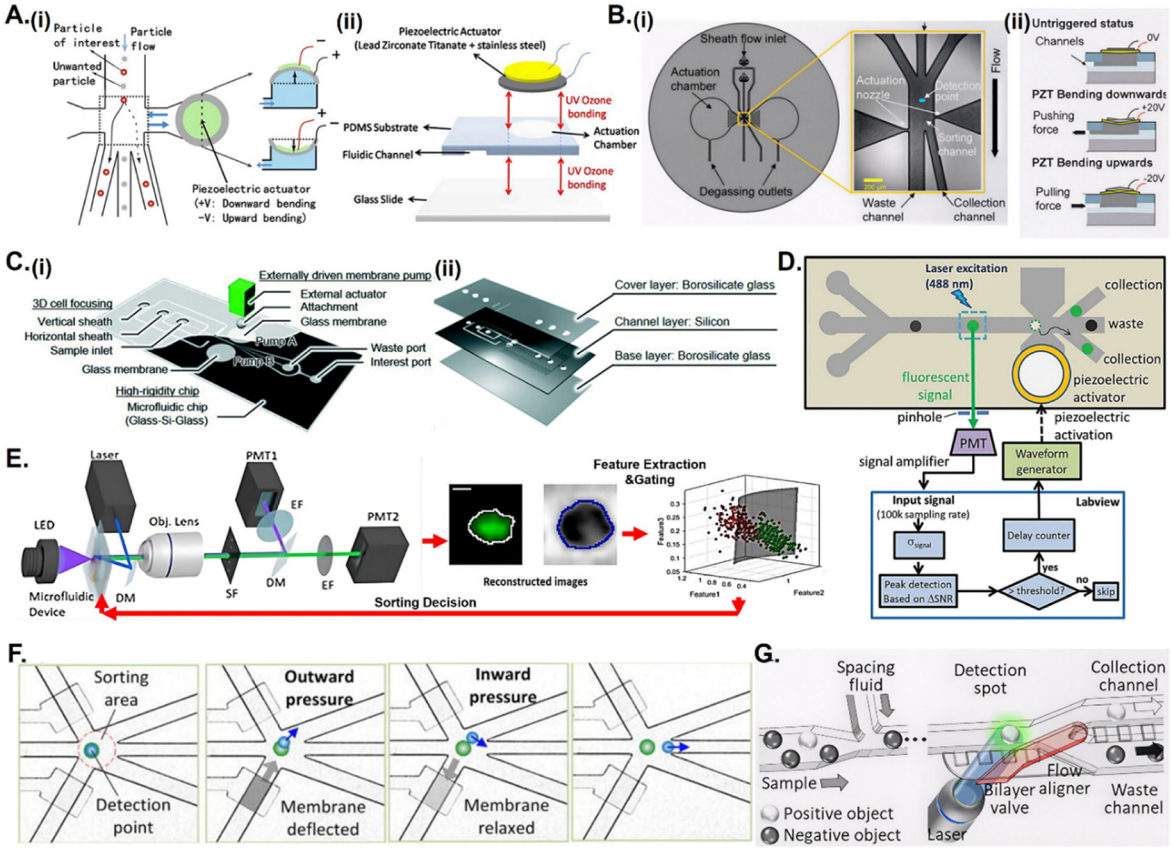

Fig. 6 Diaphragm-actuated labeled sorting platforms. (A–D) Piezoelectric (PZT) sorters: A. (i) operating principle: PZT bending under applied voltage deflects particles into side channels, while unactuated particles flow to waste, (ii) device fabricated by sequential UV-ozone bonding.[121] Reproduced from ref. 121 with permission from Springer Nature, © 2009. B. (i) Sheath-flow sorting channel with cell input and sheath streams converging at a junction, (ii) dual tapered PZT nozzles generate push–pull flows under applied voltage for active deflection.[122] Reproduced from ref. 122 with permission from Springer Nature, © 2017. C. (i) Three-layer chip design, (ii) configuration of dual diaphragm pumps, (iii) sequential actuation generating local flow for on-chip cell enrichment.[123] Reproduced from ref. 123 with permission from the Royal Society of Chemistry, © 2017. D. Low-cost μFACS integrating on-chip piezoelectric actuation with off-chip confocal fluorescence detection, PMT amplification, and electronic control for high-throughput screening.[124] Reproduced from ref. 124 with permission from Oxford University Press, © 2014. (E) Image-guided sorting (ML-triggered PZT): machine learning extracts image features from bright-field/fluorescence signals and generates gating decisions in real time, which trigger on-chip PZT actuation for high-speed, automated cell sorting.[132] Reproduced from ref. 132 with permission from John Wiley & Sons, © 2019. (F and G) Pneumatic diaphragm platforms (droplet & bilayer valves): F. (i) Setup and chip layout with actuation chambers, (ii) diaphragm-driven outward pressure diverts droplets into designated outlets.[130] Reproduced from ref. 130 with permission from AIP Publishing, © 2016. G. (i) Bilayer pneumatic valve design, (ii) diaphragm actuation modulates local trajectories, enhancing stability and sorting precision.[131] Reproduced from ref. 131 with permission from Elsevier, © 2021.

3.3.2 Label free sorting. Label-free diaphragm-actuated sorting eliminates the need for fluorescent or biochemical markers by classifying cells according to intrinsic biophysical properties including impedance spectra, morphological features, deformability, and photoacoustic response; thereby avoiding phototoxicity, staining inefficiency, and delays associated with sample preparation. These systems rely on real-time phenotyping followed by rapid diaphragm-mediated flow switching, thereby allowing high-specificity isolation of unlabeled cells while preserving throughput and mechanical gentleness. The transduction schemes that are fused with diaphragm-driven gating to trigger actuation include electrical, image-based, optical and photoacoustic. Electrical impedance-activated sorting remains one of the most mature and widely deployed label-free strategies, since it provides noninvasive, high-bandwidth electrical fingerprints of single cells. Zhang *et al.*[134] demonstrated a dual-frequency impedance cytometer (Fig. 7A) integrated with a dual-diaphragm pump, wherein FPGA or field programmable gate array-based prediction triggered sub-millisecond actuation for high-purity sorting of Jurkat and MDA-MB-231 cells with >97% purity at throughputs exceeding 1000 cells per s. Flow switching was guided by differential permittivity signatures to enable precise routing with actuation latencies under 0.3 ms. Gong *et al.*[135] developed a continuous-flow system that coupled real-time impedance bioanalysis with piezoelectrically actuated diaphragm-based jet deflection (Fig. 7B). By analyzing impedance waveform morphology to distinguish single cells from aggregates, the platform synchronized diaphragm actuation with predicted trajectory shifts and achieved high-purity, label-free sorting. These

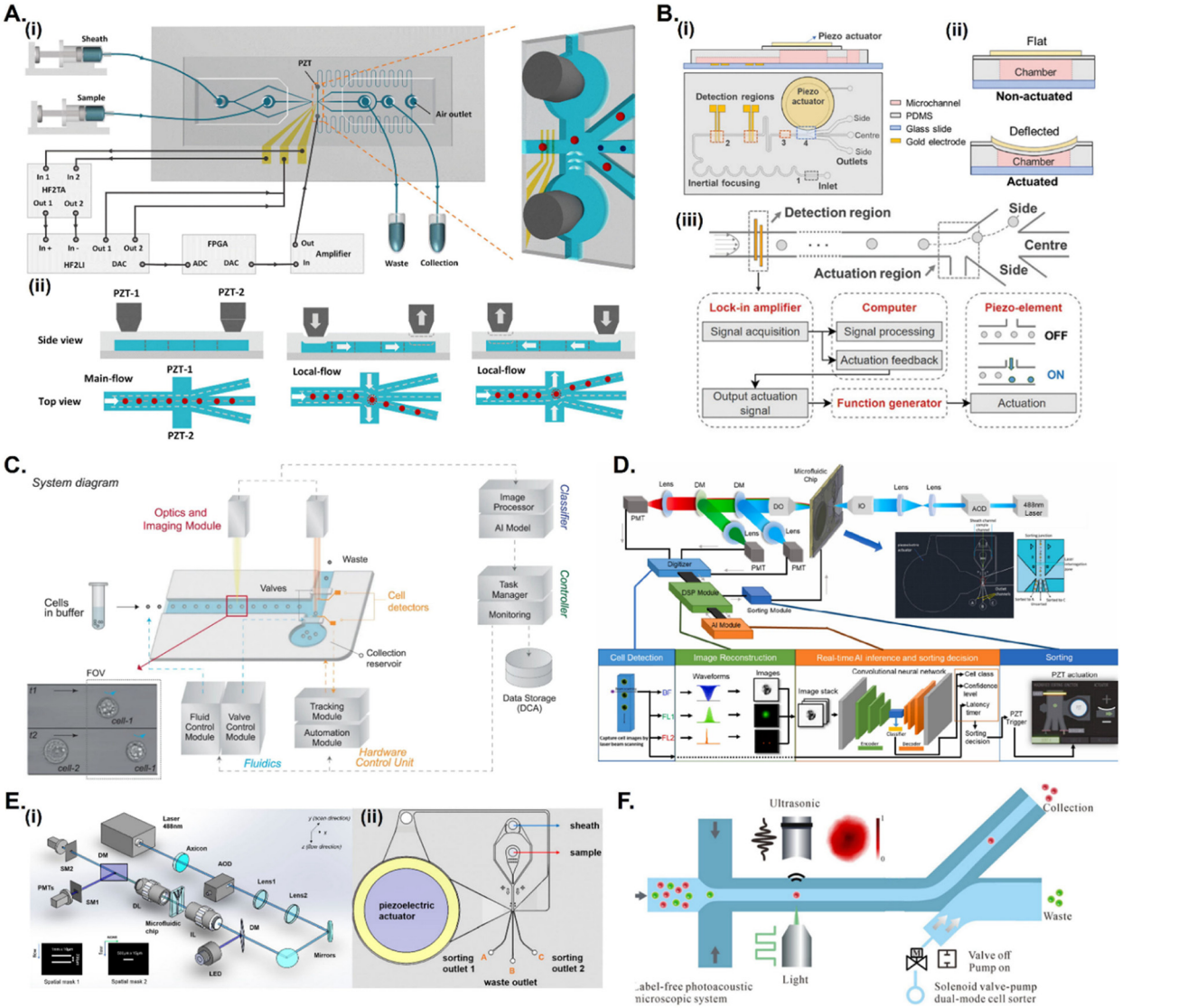

Fig. 7 Diaphragm-actuated label-free sorting platforms. (A and B) Impedance-based sorters (label-free electrical sensing): A. (i) Impedance-activated platform with dual-frequency and single-frequency operation, (ii) local flow generation *via* dual diaphragm pumps enables cell redirection.[134] Reproduced from ref. 134 with permission from the Royal Society of Chemistry, © 2024. B. (i) Device design integrating microfabricated coplanar electrodes across inlet, detection, pre-sorting, and actuation regions, (ii) piezo actuator deformation driving flow switching, (iii) impedance signal processing workflow for microcarrier sorting.[135] Reproduced from ref. 135 with permission from John Wiley & Sons, © 2024. (C–E) Intelligent AI/FPGA-driven sorters (real-time, ML/FPGA control): C. system diagram of an automated hardware-software architecture including fluidics, optics, imaging, and real-time classification modules.[137] Reproduced from ref. 137 under a CC-BY license. D. Low-latency IACS with FPGA-based reconstruction and CNN inferencing; PMT-detected bright-field/fluorescence signals are processed in real time to trigger on-chip PZT actuation.[138] Reproduced from ref. 138 under a CC-BY license. E. (i) Optical imaging setup with AOD, DM, and spatial masks for cell speed and transmission imaging, (ii) injection-molded COC microfluidic chip design.[140] Reproduced from ref. 140 under a CC-BY license. (F) Photoacoustic sorters: opto-acousto-fluidic system for microalgae sorting, integrating photoacoustic microscopy for label-free AXT detection with solenoid valve-pump actuation for high-throughput sorting.[139] Reproduced from ref. 139 with permission from the American Chemical Society, © 2024.

approaches highlight how electrical phenotyping can trigger diaphragm motion with sub-millisecond precision, thereby enabling high-speed discrimination of cell states such as viability, biomass, or differentiation status without the need for labels.

Image-activated sorting forms the second major class of label-free diaphragm systems, leveraging brightfield morphology, size, texture, or deformation signatures to inform actuation. Yu *et al.*[136] presented a dual-mode approach combining brightfield imaging for morphological classification with fluorescence validation, using diaphragm-triggered deflection to isolate budding yeast cells with high fidelity, thereby demonstrating the feasibility of multimodal detection-actuation integration in real-time. Complementarily, Salek *et al.*[137] introduced the COSMOS platform (Fig. 7C), which utilized high-framerate brightfield imaging and deep convolutional neural networks to generate

latent feature embedding of flowing cells to dynamically inform pneumatic valve actuation for morphology-guided label-free sorting of cancerous and primary cell populations. Tang *et al.*[138] extended this paradigm by integrating brightfield shape recognition and aspect-ratio analysis into a logic-driven microvalve array (Fig. 7D), wherein diaphragm actuation was triggered by real-time deformation cues, thereby enabling stain-free enrichment of circulating tumor cells directly from whole blood. Together, these systems demonstrate how diaphragm-based flow control can be tightly synchronized with machine-vision classifiers to isolate phenotypes that cannot be distinguished electrically or *via* simple optical thresholds.

Beyond electrical and imaging modalities, diaphragm-integrated platforms have also incorporated acoustics, photoacoustics, and Raman spectroscopy to enable content-specific, chemical-level discrimination without labels. Duan *et al.*[139] developed a photoacoustic microscopy driven sorter that identified astaxanthin-rich *Haematococcus pluvialis* through light-absorption induced intracellular photoacoustic resonance, triggering solenoid-actuated diaphragm valves for high-value bioresource enrichment with a 4.38× concentration gain (Fig. 7F). Chen *et al.*[140] introduced a label-free image-guided system using a scanning Bessel–Gaussian beam to generate high-fidelity transmission waveforms encoding morphological and subcellular features of unlabeled cells (Fig. 7E), with a piezoelectric diaphragm actuator performing real-time sorting based on waveform-derived classification parameters. Nitta *et al.*[141] developed a Raman image-activated cell sorting (RIACS) platform that measured chemically specific intracellular vibrations using multicolor stimulated Raman scattering microscopy and coupled these signals to a dual-membrane push–pull diaphragm sorter driven by an FPGA-CPU processor, enabling spatially resolved molecular sorting (~50 events per s) without reliance on fluorescent staining. These modalities expand diaphragm actuation into regimes wherein intracellular composition and molecular structure determine the sorting decisions for specific discrimination in label-free workflows. However, while label-free diaphragm-based sorting systems avoid staining artifacts and preserve sensitive phenotypes, they remain susceptible to noise within impedance measurements, variability in image-based classifiers, and slower response when pneumatic elements dominate the actuation. Current throughputs (10^2–10^3 cells per s) are improving but still trail the tens-of-kHz rates achievable with marker-dependent or cavitation-based systems. Nevertheless, diaphragm-mediated switching provides gentle hydrodynamic handling and direct compatibility with Raman, impedance, or ML-based classifiers, making it particularly suitable for fragile, rare, or clinically unmodified cells. Recent advances in FPGA-accelerated gating and CNN-guided morphology recognition demonstrate that sub-millisecond classification-actuation loops are feasible, positioning diaphragm-actuated platforms as a uniquely adaptable route to high-content, label-free cytometry beyond the capabilities of conventional acoustic or dielectrophoretic methods.

3.3.3 Hybrid sorting. Hybrid diaphragm-actuated platforms merge label-based and label-free modalities within a single architecture to enable sorting that alternates between fluorescence-based decisions and intrinsic biophysical metrics such as electrical pulses or image-derived features. In these systems, the diaphragm serves as the common physical routing element, thereby allowing different sensing channels to trigger the same actuation pathway without modifying the underlying microfluidic geometry. This capability is increasingly valuable for workflows wherein the sample identity, staining constraints, or analytical goals vary from run to run. Rajauria *et al.*[87] demonstrated this principle using a push–pull piezoelectric diaphragm that could respond either to resistive pulse sensing (RPS) signals for label-free, size-based discrimination or to fluorescence triggers for tagged particles and mammalian cells (Fig. 8A). By allowing both modalities to drive the same diaphragm-based jet-deflection mechanism, the system achieved >95% fidelity at throughputs approaching 60 000 particles per minute while maintaining gentle handling compatible with fragile samples. Nitta *et al.*[142] expanded the concept by integrating brightfield and fluorescence imaging with deep-learning classification and dual piezoelectric diaphragm actuators (Fig. 8B), enabling the same device to sort cells by molecular tags or by label-free morphological signatures. Here, the diaphragm functions as a fast mechanical switch downstream of a software-defined decision layer, allowing the sorter to route cells based on fluorescence intensities when available or CNN-derived brightfield embeddings when labels are undesirable. This multimodal flexibility enables tasks such as identifying protein localization patterns or aggregative behaviours that exceed the capabilities of purely labeled or purely label-free systems. Although hybrid platforms offer unmatched adaptability, they require careful coordination between sensing pipelines and diaphragm timing, increasing control complexity and reducing throughput relative to single-mode systems. Even so, they demonstrate how diaphragm actuation can unify disparate detection modalities into a compact, reconfigurable cytometry framework that toggles between affinity-tagged and intrinsic biophysical metrics according to experimental need.

Taken together, the diaphragm-actuated sorting platforms in section 3.3 show how a single mechanical framework can support three complementary cytometry modes: marker-dependent label-based sorting, label-free discrimination, and hybrid multimodal operation (Table 4). Marker-dependent systems leverage fluorescence or affinity tags to achieve high specificity at up to kHz-scale throughputs, but remain constrained by phototoxicity, staining requirements, and sample prep overhead. Label-free platforms instead exploit intrinsic signatures including impedance spectra, morphology, deformation, photoacoustic or Raman responses, coupled to diaphragm-triggered flow switching, thereby offering gentler handling and access to native phenotypes at the cost of greater sensitivity to signal noise and typically lower throughput. Hybrid systems use the diaphragm as a unified routing element downstream of electrical, optical, and machine-learning classifiers, enabling the same device to toggle between labeled and label-free criteria as experimental needs change, albeit with

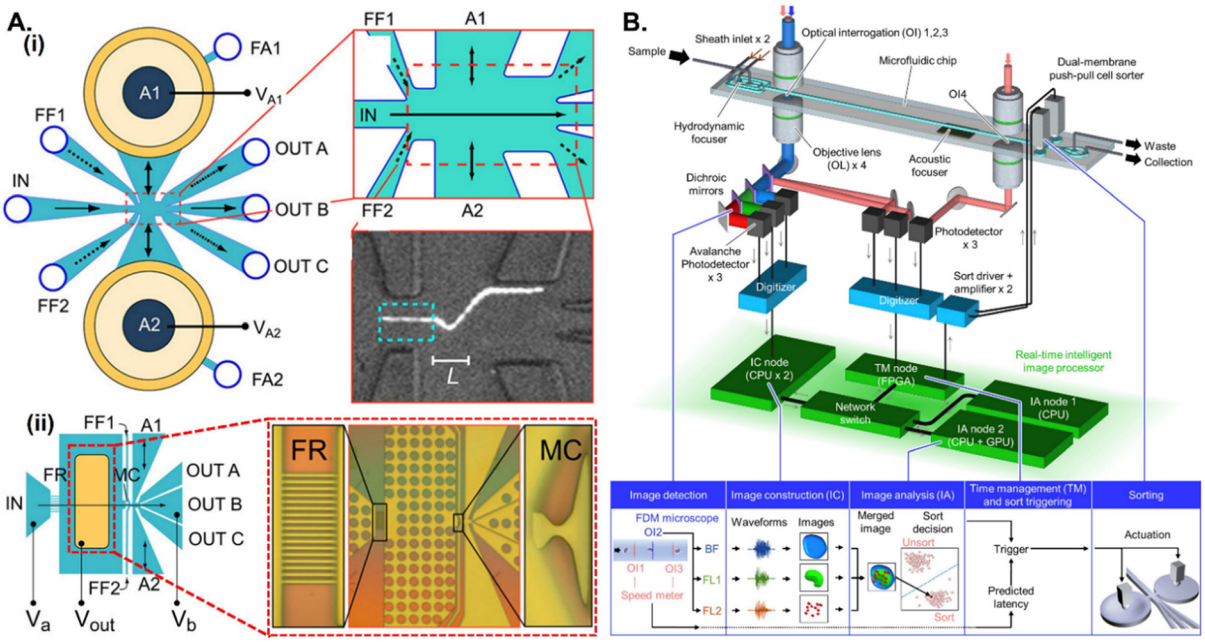

Fig. 8 Diaphragm-actuated hybrid sorting platforms. A. Dual-mode device combining (i) fluorescence (CCD) and label-free (ii) resistive pulse sensing (RPS) for particle classification; diaphragm actuators redirect focused streams into three outlets.[87] Reproduced from ref. 87 with permission from the American Chemical Society, © 2015. B. Intelligent automated cell sorter (IACS) integrates hydrodynamic and acoustic focusing with real-time image analysis, triggering dual-membrane push–pull sorting for fully automated operation[142] reproduced from ref. 142 with permission from the Elsevier, © 2018.

added computational and control complexity. Across all modes, the key opportunity lies in tighter integration of high-speed decision electronics (FPGA/CNN-based inference), low-latency actuation, and robust microfluidic architectures, so that diaphragm-based sorters can deliver scalable, high-content cytometry that complements or exceeds the capabilities of conventional FACS, acoustic, or dielectrophoretic approaches.

4 Discussion and future directions

Diaphragm-actuated microfluidic systems have shown considerable promise for sample enrichment and activated sorting, leveraging their ability to provide highly controllable fluidic manipulation, programmable compartmentalization, and real-time sample processing within compact platforms. As these technologies mature, the dual utility of diaphragm actuation for selective analyte pre-concentration and for dynamic cell per particle routing places them at the forefront of next-generation lab-on-a-chip platforms. However, targeted innovation is required to overcome current limitations and to extend the capabilities beyond current boundaries in throughput, sensitivity, specificity, and operational robustness.

4.1 Material innovations for robust performance

One major direction of development lies in materials optimization for repeated, high-frequency diaphragm operation during enrichment and sorting cycles. While PDMS-based diaphragms offer mechanical flexibility and ease of integration; their long-term actuation metrics, particularly under rapid cycling in the context of sorting or sustained pressure gradients in sample enrichment workflows leads to fatigue, shape-memory hysteresis, and fouling, especially while processing complex biological samples. Composite elastomers reinforced with nanomaterials (*e.g.*, carbon nanotubes or aramid nanofibers) are being explored to enhance fatigue resistance, while maintaining sufficient flexibility for the large deflection amplitudes required for particle gating or bead-trap collapse.[143–145] Moreover, the antifouling behavior of hybrid hydrogel–elastomer interfaces[146,147] or zwitterionic surface coatings[148] could be particularly beneficial for maintaining high sorting fidelity and capture efficiency, especially while operating with blood, serum, or wastewater samples. These advances are critical for ensuring consistent enrichment efficiency and sorting accuracy over prolonged operation, especially in high-throughput or automated contexts.

4.2 Emerging actuation modalities and real-time control

From an actuation standpoint, while pneumatic and piezoelectric diaphragms dominate current enrichment and sorting designs due to their well-characterized performance and fabrication compatibility, emerging hybrid modalities are expanding how membrane deformation can be driven, with the potential to improve precision, responsiveness, and integration flexibility of sorting and trapping functions. For enrichment, magnetically actuated diaphragms embedded with soft magnetic particles allow localized and remote modulation of trap zones without physical tethering, thereby freeing the moving membrane from mechanical connection to external pumps, springs, or levers. Eliminating these rigid couplings reduces device bulk, simplifies

packaging, and facilitates fully enclosed cartridges, which are highly advantageous in portable point-of-care devices wherein compactness and mechanical robustness are critical.[149,150] For sorting, photoactuated[151,152] or electrostatic[153,154] diaphragm elements provide ultrafast flow switching with minimal footprint, supporting rapid, low-energy deformation and high-purity, high-speed discrimination of target analytes or cells in single or multichannel arrays. Future research should focus on optimizing the coupling efficiency between actuation stimulus and diaphragm deflection, and on implementing real-time feedback mechanisms such as integrated displacement sensing, piezoresistive elements, or flow-based pressure monitoring to dynamically adjust actuation profiles in response to sample characteristics or sensor readouts.

4.3 Sensor-integrated actuation for intelligent operation

The integration of diaphragm actuation with real-time detection continues to be a key enabling feature within enrichment and activated sorting approaches. In enrichment platforms, the timing and magnitude of diaphragm collapse directly determine which affinity beads experience localized compression, thereby allowing selective trapping and controlled release of bead matrices without exposing the broader channel to unwanted flow disturbances. This coordinated compression enhances the capture efficiency of low-abundance targets such as extracellular vesicles, nucleic acids, or rare pathogens by increasing their residence time within the confined reaction space. Future platforms will likely benefit from sensor-triggered actuation schemes, wherein diaphragm movement is initiated only upon confirmation of binding events, using impedance,[155] fluorescence,[66,156] or mass-sensitive detection[157] to provide automated, condition-dependent activation. In sorting systems, especially those relying on label-free modalities, rapid synchronization between detection and diaphragm-induced flow deflection is essential. As diaphragm motion physically redirects streamlines, the actuation must occur within milliseconds of target identification to ensure the cell or particle has not passed the diversion point. Innovations in AI-guided image classification,[158] differential impedance profiling,[159] and Raman scattering-based detection[160] are pushing the boundaries of what can be recognized in real time, thereby increasing the informational content available for decision-making and placing greater demands on actuation latency. FPGA-based control architectures and neuromorphic edge processing are emerging solutions for reducing the delay between detection and diaphragm movement, thereby maintaining sorting fidelity, even as throughput and feature-recognition speeds continue to rise.[161,162]

4.4 Confinement-enhanced detection sensitivity

While diaphragm-based microfluidics are largely discussed in the context of enrichment and sorting, an equally important capability is their ability to enhance detection sensitivity by mechanically reshaping the sensing region. By actively modulating the local channel cross-section, these membranes increase the fraction of the interrogation volume displaced by a transiting particle or cell, amplifying electrical or optical signals relative to baseline noise. This confinement-enhanced response is particularly effective in impedance cytometry and resistive-pulse sensing, wherein signal magnitude scales with the fractional change in channel volume during translocation. Pneumatically actuated PDMS membranes integrated over sensing electrodes have been used to dynamically tune the detection volume in real time. Riordon *et al.*[163] demonstrated that increasing actuation pressure reduced the channel volume to approximately 2% of its original size, boosting the signal-to-noise ratio for 7.3 μm beads from ~69 to ~190 and enabling detection of *E. coli* cells near the original measurement threshold. Similarly, Huang *et al.*[164] incorporated a pneumatically driven PDMS membrane at a constricted sensing zone for single-cell impedance spectroscopy, thereby allowing the constriction to be adjusted to improve sensitivity while mitigating clogging. This approach enabled accurate extraction of single-cell membrane capacitance (~2.17 μF cm^{-2}) and cytoplasm conductivity (~0.74 S m^{-1}) across 1–100 kHz.[164] Julian *et al.*[165] further showed that mechanically compressing a PDMS channel to reduce height by one-third produced a 3.2-fold increase in impedance amplitude for 6 μm beads, doubled the signal-to-noise ratio at 1 and 6 MHz, and enabled discrimination of yeast from beads under clog-resistant, real-time operation. Stepping beyond PDMS, tunable resistive-pulse sensing (TRPS) platforms employ elastomeric membranes with stretchable nanopores whose size can be precisely adjusted. Sowerby *et al.*[166] showed that reducing the pore diameter in a polyurethane membrane increased ionic blockade amplitudes for particles ranging from viruses to extracellular vesicles, thereby improving the limit of detection. Willmott *et al.*[167] further quantified this effect for 200–800 nm polystyrene beads, demonstrating that smaller pore openings elevated signal amplitudes sufficiently to detect particles previously buried in baseline noise. These findings suggest that membrane deflection can be systematically incorporated into next-generation enrichment and sorting platforms as a tuneable sensitivity-control element, complementing the upstream and downstream mechanisms responsible for particle handling. By providing real-time adjustment of the local sensing geometry, such deformable membranes can support adaptive detection thresholds that respond to particle size, flow variability, or noise conditions, thereby improving measurement fidelity across heterogeneous samples. When integrated within broader microfluidic architectures, this capability could be particularly powerful, in combination with AI-driven classification frameworks, thereby enabling closed-loop operation in which sensing conditions adapt dynamically to optimize signal quality and overall system performance.

4.5 Multifunctionality and scalability in platform design

Scalability and multifunctionality are emerging criteria within sensing for biomanufacturing workflows. Many diaphragm-

based enrichment and sorting platforms remain single-function or single-channel, limiting their applicability in multi-analyte diagnostics or integrated workflows. Modular microfluidic architectures, in which diaphragm valves are reconfigurable or multiplexed, offer a path toward greater versatility. For instance, programmable enrichment chambers could be toggled between different affinity bead types by spatiotemporally modulated diaphragm actuation to enable sequential capture of multiple biomarkers within a single assay.[108,168] In sorting functions, diaphragm-integrated arrays capable of executing conditional logic based on cell phenotype, or deformability[169] can enable complex sorting hierarchies, such as subpopulation isolation or exclusion of undesired cell clusters. Furthermore, combining sorting with on-chip post-processing such as cell lysis, isothermal amplification, or immunostaining can be facilitated through the fluidic control enabled by multilayer diaphragm-based systems.

4.6 Adaptation to complex sample matrices

A significant frontier for enrichment and sorting is the adaptation of diaphragm-based systems to real-world sample types. Biological and environmental matrices often contain particulates, proteins, and debris that rapidly clog microchannels or compromise valve integrity. Diaphragm designs that emphasize self-clearing behaviour, such as dynamic peristaltic pumping, pulsatile membrane flexing could improve operational stability under such conditions. Additionally, the ability to tune diaphragm actuation frequency and amplitude in real time based on flow resistance or detection signals[170] may offer a means to adapt sorting gates or enrichment zones dynamically, thereby preserving performance despite fluctuating sample quality. Integration of soft, deformable membranes with nanoconfined reaction zones is also promising for increasing binding kinetics,[106,107] especially when combined with active mixing induced by cyclical diaphragm motion.[108]

4.7 Manufacturing, standardization, and clinical translation

As the field moves toward deployment, standardization and manufacturability become pressing issues. For enrichment and sorting platforms to be adopted in clinical diagnostics, bioprocessing, or environmental monitoring, they must be produced at scale with minimal performance variability. While soft lithography remains dominant in research prototyping, advances in high-resolution 3D printing[171] and injection molding of thermoplastic elastomers[172] are enabling diaphragm features to be manufactured in reproducible formats suitable for mass production. The use of single-material multilayer architectures, solvent-free bonding techniques, and low-cost actuation modules (*e.g.*, paper-based pneumatic pumps[173] or smartphone-controlled piezo drivers[174]) will further accelerate deployment in low-resource settings.

5 Conclusions

Diaphragm-actuated microfluidic platforms occupy a uniquely powerful position for multifunctional sample enrichment and sorting due to their reconfigurable nature, integration ability with diverse sensing schemes, and adaptability to real-time control. By integrating advances in materials engineering, actuation dynamics, and intelligent detection, these platforms are poised to evolve into fully autonomous sample-to-answer systems capable of operating in decentralized, high-throughput, or even wearable formats. Emerging areas include novel fatigue resistant diaphragm materials, sensor-integration for real-time control, and utilization of artificial intelligence (AI) approaches to harness multimodal information to trigger actuation. Future research should thus focus on the holistic co-design of diaphragm materials, actuator mechanics, and detection interfaces to meet the stringent demands of point-of-care diagnostics, rare-cell isolation, single-vesicle capture, and environmental contaminant monitoring; domains wherein high sensitivity, specificity, and adaptability are non-negotiable.

Author contributions

A.-B. S.: conceptualization, formal analysis, visualization, writing – original draft, review & editing. S. M.: visualization. N. S. S.: conceptualization, writing – review & editing, supervision, funding acquisition and project administration.

Conflicts of interest

The authors have no conflict of interest related to this work.

Data availability

The data presented in this review were obtained from publicly available sources, including PubMed, Web of Science, Google Scholar and various journal databases. All relevant data can be accessed through the citations provided within the review.

Acknowledgements

This work was supported by the NCI Grants P30 CA44579 and U54 CA274499, AFOSR grants FA9550-24-1-0057, FA9550-21-1-0430 & FA2386-21-1-4070 and the University of Virginia's Paul Manning Launchpad for Diabetes Research Program.

References

1 G. M. Whitesides, *Nature*, 2006, **442**, 368–373.
2 T. M. Squires and S. R. Quake, *Rev. Mod. Phys.*, 2005, **77**, 977–1026.
3 C. L. Hansen, E. Skordalakes, J. M. Berger and S. R. Quake, *Proc. Natl. Acad. Sci. U. S. A.*, 2002, **99**, 16531–16536.
4 C. W. Shields Iv, C. D. Reyes and G. P. López, *Lab Chip*, 2015, **15**, 1230–1249.

5 G. A. Cooksey, S. Iavarone-Garza, N. Drachman and P. N. Patrone, *Meas.: Sens.*, 2025, **38**, 101548.
6 R. H. Cole, S.-Y. Tang, C. A. Siltanen, P. Shahi, J. Q. Zhang, S. Poust, Z. J. Gartner and A. R. Abate, *Proc. Natl. Acad. Sci. U. S. A.*, 2017, **114**, 8728–8733.
7 S. Nagrath, L. V. Sequist, S. Maheswaran, D. W. Bell, D. Irimia, L. Ulkus and M. Toner, *Nature*, 2007, **450**, 1235–1239.
8 T. Yeo, S. J. Tan, C. L. Lim, D. P. X. Lau, Y. W. Chua, S. S. Krisna and C. T. Lim, *Sci. Rep.*, 2016, **6**, 22076.
9 S. R. Doonan, M. Lin and R. C. Bailey, *Lab Chip*, 2019, **19**, 1589–1598.
10 K. Torres-Castro, J. Jarmoshti, L. Xiao, A. Rane, A. Salahi, L. Jin, X. Li, F. Caselli, C. Honrado and N. S. Swami, *Adv. Mater. Technol.*, 2023, **8**, 2201463.
11 D. Di Carlo, *Lab Chip*, 2009, **9**, 3038–3046.
12 L. R. Huang, E. C. Cox, R. H. Austin and J. C. Sturm, *Science*, 2004, **304**, 987–990.
13 J. McGrath, M. Jimenez and H. Bridle, *Lab Chip*, 2014, **14**, 4139–4158.
14 J. M. Martel and M. Toner, *Annu. Rev. Biomed. Eng.*, 2014, **16**, 371–396.
15 J. Zhang, S. Yan, D. Yuan, G. Alici, N. T. Nguyen, M. E. Warkiani and W. Li, *Lab Chip*, 2016, **16**, 10–34.
16 S. Mirhosseini, M. Eskandarisani, A. Faghih Nasiri, F. Khatami, A. Mirzaei, M. Badieirostami, S. M. K. Aghamir and M. Kolahdouz, *Biosensors*, 2024, **14**(10), 466.
17 N. Pamme, *Lab Chip*, 2006, **6**, 24–38.
18 N. Pamme and C. Wilhelm, *Lab Chip*, 2006, **6**, 974–980.
19 T. Laurell, F. Petersson and A. Nilsson, *Chem. Soc. Rev.*, 2007, **36**, 492–506.
20 S. Yaman, M. Anil-Inevi, E. Ozcivici and H. C. Tekin, *Front. Bioeng. Biotechnol.*, 2018, **6**, 192.
21 V. Farmehini, S. Kiendzior, J. P. Landers and N. S. Swami, *ACS Sens.*, 2021, **6**, 3765–3772.
22 A. Rane, J. Jarmoshti, A. B. Siddique, S. Adair, K. Torres-Castro, C. Honrado and N. S. Swami, *Lab Chip*, 2024, **24**, 561–571.
23 R. Pethig, *Biomicrofluidics*, 2010, **4**, 022811.
24 J. Jarmoshti, A.-B. Siddique, A. Rane, A. R. Hyler, S. Adair, T. W. Bauer and N. S. Swami, *ACS Sens.*, 2025, **10**, 4116–4126.
25 A. T. Lau, H. M. Yip, K. C. Ng, X. Cui and R. H. Lam, *Micromachines*, 2014, **5**, 50–65.
26 J. Kim, M. Kang, E. C. Jensen and R. A. Mathies, *Anal. Chem.*, 2012, **84**, 2067–2071.
27 R. T. Kelly, C. Wang, S. J. Rausch, C. S. Lee and K. Tang, *Anal. Chem.*, 2014, **86**, 6723–6729.
28 B. Sabbagh, S. Park and G. Yossifon, *Anal. Chem.*, 2023, **95**, 6514–6522.
29 A. Wolff, I. R. Perch-Nielsen, U. D. Larsen, P. Friis, G. Goranovic, C. R. Poulsen and P. Telleman, *Lab Chip*, 2003, **3**, 22–27.
30 T. Thorsen, S. J. Maerkl and S. R. Quake, *Science*, 2002, **298**, 580–584.
31 J. Kim, A. M. Stockton, E. C. Jensen and R. A. Mathies, *Lab Chip*, 2016, **16**, 812–819.
32 J. D. Tice, J. B. Rosheck, C. D. Hamlin, C. A. Apblett and P. J. Kenis, *J. Microelectromech. Syst.*, 2013, **22**, 1251–1253.
33 A. C. Atik, M. D. Özkan, E. Özgür, H. Külah and E. Yıldırım, *J. Micromech. Microeng.*, 2020, **30**, 115001.
34 I. V. Uvarov, M. V. Lokhanin, A. V. Postnikov, A. E. Melenev and V. B. Svetovoy, *Sens. Actuators, B*, 2018, **260**, 12–20.
35 I. E. Araci and S. R. Quake, *Lab Chip*, 2012, **12**, 2803–2806.
36 J. P. Urbanski, W. Thies, C. Rhodes, S. Amarasinghe and T. Thorsen, *Lab Chip*, 2006, **6**, 96–104.
37 A. K. White, M. VanInsberghe, O. I. Petriv, M. Hamidi, D. Sikorski, M. A. Marra, J. Piret, S. Aparicio and C. L. Hansen, *Proc. Natl. Acad. Sci. U. S. A.*, 2011, **108**, 13999–14004.
38 C. J. Easley, J. M. Karlinsey, J. M. Bienvenue, L. A. Legendre, M. G. Roper, S. H. Feldman, M. A. Hughes, E. L. Hewlett, T. J. Merkel, J. P. Ferrance and J. P. Landers, *Proc. Natl. Acad. Sci. U. S. A.*, 2006, **103**, 19272–19277.
39 Z. Hua, Y. Xia, O. Srivannavit, J. M. Rouillard, X. Zhou, X. Gao and E. Gulari, *J. Micromech. Microeng.*, 2006, **16**, 1433.
40 W. H. Grover, M. G. von Muhlen and S. R. Manalis, *Lab Chip*, 2008, **8**, 913–918.
41 W. H. Grover, A. M. Skelley, C. N. Liu, E. T. Lagally and R. A. Mathies, *Sens. Actuators, B*, 2003, **89**, 315–323.
42 Y. Tanaka, *RSC Adv.*, 2013, **3**, 10213–10220.
43 K. Ren, W. Dai, J. Zhou, J. Su and H. Wu, *Proc. Natl. Acad. Sci. U. S. A.*, 2011, **108**, 8162–8166.
44 S. Messner, J. Schaible, H. Sandmaier and R. Zengerle, *Microfluid. Nanofluid.*, 2006, **2**, 89–96.
45 I. V. Uvarov, P. S. Shlepakov, A. E. Melenev, K. Ma, V. B. Svetovoy and G. J. M. Krijnen, *Actuators*, 2021, **10**(3), 62.
46 T. Salafi, Y. Zhang and Y. Zhang, *Nanomicro Lett.*, 2019, **11**, 77.
47 Q. Zhao, D. Yuan, J. Zhang and W. Li, *Micromachines*, 2020, **11**, 461.
48 D. Jiang, C. Ni, W. Tang, D. Huang and N. Xiang, *Biomicrofluidics*, 2021, **15**, 041501.
49 N. Abd Rahman, F. Ibrahim and B. Yafouz, *Sensors*, 2017, **17**, 449.
50 P. Zhang, H. Bachman, A. Ozcelik and T. J. Huang, *Annu. Rev. Anal. Chem.*, 2020, **13**, 17–43.
51 Y. Gao, M. Wu, Y. Lin and J. Xu, *Micromachines*, 2020, **11**, 921.
52 J. Y. Qian, C. W. Hou, X. J. Li and Z. J. Jin, *Micromachines*, 2020, **11**, 172.
53 N. El-Atab, R. B. Mishra, F. Al-Modaf, L. Joharji, A. A. Alsharif, H. Alamoudi and M. M. Hussain, *Adv. Intell. Syst.*, 2020, **2**, 2000128.
54 A. Mata, A. J. Fleischman and S. Roy, *Biomed. Microdevices*, 2005, **7**, 281–293.
55 Y. Yu, D. Sanchez and N. Lu, *J. Mater. Res.*, 2015, **30**, 2702–2712.
56 K. J. Regehr, M. Domenech, J. T. Koepsel, K. C. Carver, S. J. Ellison-Zelski, W. L. Murphy and D. J. Beebe, *Lab Chip*, 2009, **9**, 2132–2139.
57 W. A. Laftah, W. A. W. A. Rahman and A. N. Ibrahim, *RSC Adv.*, 2025, **15**, 14838–14847.

58 S. Noimark, R. J. Colchester, B. J. Blackburn, E. Z. Zhang, E. J. Alles, S. Ourselin and A. E. Desjardins, *Adv. Funct. Mater.*, 2016, **26**, 8390–8396.
59 K. Song, N. K. Cho, Y. Choi, S. Connolly and H. J. Nam, *Polymer*, 2024, **290**, 126552.
60 S. Zhuo, A. Zhang, A. Tessier, C. Williams and S. Kabiri Ameri, *Biosensors*, 2024, **14**, 188.
61 J. Vaicekauskaite, P. Mazurek, S. Vudayagiri and A. L. Skov, *J. Mater. Chem. C*, 2020, **8**, 1273–1279.
62 A. Hamidi and Y. Tadesse, *Mater. Des.*, 2020, **187**, 108324.
63 G. Scetta, J. Ju, N. Selles, P. Heuillet, M. Ciccotti and C. Creton, *J. Polym. Sci.*, 2021, **59**, 685–696.
64 J. Ortigoza-Diaz, K. Scholten, C. Larson, A. Cobo, T. Hudson, J. Yoo and E. Meng, *Micromachines*, 2018, **9**, 422.
65 S. K. Lee, M. G. Kim, J. Y. An, M. H. Jun, S. Yang and J. H. Lee, in *2009 IEEE 22nd International Conference on Micro Electro Mechanical Systems*, 2009, pp. 955–958.
66 W. Hilber, *Appl. Phys. A: Mater. Sci. Process.*, 2016, **122**, 751.
67 I. Stachiv, E. Alarcon and M. Lamac, *Metals*, 2021, **11**, 415.
68 V. Belwanshi, K. Rane, V. Kumar and B. Pramanick, *Micromachines*, 2023, **14**, 1725.
69 R. Khakpour, S. R. M. Mansouri and A. R. Bahadorimehr, in *2010 International Conference on Electronic Devices, Systems and Applications*, 2010, pp. 297–299.
70 M. A. Unger, H. P. Chou, T. Thorsen, A. Scherer and S. R. Quake, *Science*, 2000, **288**, 113–116.
71 A. Lima-Rodriguez, J. Garcia-Manrique, W. Dong and A. Gonzalez-Herrera, *Membranes*, 2022, **12**, 288.
72 S. Ma, K. Yang, S. Wang, H. Liu, X. Zhou and M. Li, *J. Appl. Phys.*, 2021, **130**, 024504.
73 J. A. Miguel, Y. Lechuga and M. Martinez, *Micromachines*, 2018, **9**, 342.
74 S. K. Jindal, A. Mahajan and S. K. Raghuwanshi, *Microsyst. Technol.*, 2016, **22**, 1143–1150.
75 M. Dorfmeister, M. Schneider and U. Schmid, *Sens. Actuators, A*, 2018, **282**, 259–268.
76 Y. Chi, Y. Li, Y. Zhao, Y. Hong, Y. Tang and J. Yin, *Adv. Mater.*, 2022, **34**, 2110384.
77 H. B. Khaniki, M. H. Ghayesh, R. Chin and M. Amabili, *Nonlinear Dyn.*, 2022, **110**, 963–994.
78 P. S. Lin, O. Le Roux de Bretagne, M. Grasso, J. Brighton, C. StLeger-Harris and O. Carless, *Designs*, 2023, **7**, 135.
79 T. K. Kim, J. K. Kim and O. C. Jeong, *Microelectron. Eng.*, 2011, **88**, 1982–1985.
80 E. Yang, M. Zhang, J. Zeng and F. Tian, *Soft Matter*, 2022, **18**, 5465–5473.
81 J. A. Voorthuyzen and P. Bergveld, *Sens. Actuators*, 1984, **6**, 201–213.
82 M.-H. Bao, in *Handbook of Sensors and Actuators*, ed. M.-H. Bao, Elsevier Science B.V., 2000, vol. 8, pp. 23–88.
83 C. E. Imrak and I. Gerdemeli, *Appl. Math. Sci.*, 2007, **1**, 2129–2137.
84 K. Hosokawa and R. Maeda, *J. Micromech. Microeng.*, 2000, **10**, 415.
85 S. E. Hulme, S. S. Shevkoplyas and G. M. Whitesides, *Lab Chip*, 2009, **9**, 79–86.
86 C. Huang, Y. Jiang, Y. Li and H. Zhang, *Micromachines*, 2022, **14**, 103.
87 S. Rajauria, C. Axline, C. Gottstein and A. N. Cleland, *Nano Lett.*, 2015, **15**, 469–475.
88 F. Lickert, M. Ohlin, H. Bruus and P. Ohlsson, *J. Acoust. Soc. Am.*, 2021, **149**, 4281–4291.
89 H. Conrad, H. Schenk, B. Kaiser, S. Langa, M. Gaudet, K. Schimmanz and M. Lenz, *Nat. Commun.*, 2015, **6**, 10078.
90 A. V Desai, J. D. Tice, C. A. Apblett and P. J. Kenis, *Lab Chip*, 2012, **12**, 1078–1088.
91 J. K. Hamilton, M. T. Bryan, A. D. Gilbert, F. Y. Ogrin and T. O. Myers, *Sci. Rep.*, 2018, **8**, 933.
92 J. A. Potkay and K. D. Wise, *Micromachines*, 2012, **3**, 379–395.
93 K. Abi-Samra, L. Clime, L. Kong, R. Gorkin III, T. H. Kim, Y. K. Cho and M. Madou, *Microfluid. Nanofluid.*, 2011, **11**, 643–652.
94 S. Basak and P. De, *ChemistrySelect*, 2025, **10**, e01828.
95 A. Dana, S. Vollach and D. Shilo, *Actuators*, 2021, **10**(7), 140.
96 D. Satoh, S. Tanaka and M. Esashi, *IEEJ Trans. Electr. Electron. Eng.*, 2008, **3**, 305–312.
97 F. Perdigones, A. Luque and J. M. Quero, *Micro Nano Lett.*, 2011, **6**, 363–365.
98 H. J. Choi, G. Ahn, U. S. Yu, E. J. Kim, J. Y. Ahn and O. Chan Jeong, *ACS Omega*, 2023, **8**, 28344–28354.
99 D. C. Leslie, C. J. Easley, E. Seker, J. M. Karlinsey, M. Utz, M. R. Begley and J. P. Landers, *Nat. Phys.*, 2009, **5**, 231–235.
100 H. Sano, Y. Kazoe, K. Morikawa and T. Kitamori, *J. Micromech. Microeng.*, 2023, **33**, 085007.
101 C. H. Chiou, T. Y. Yeh and J. L. Lin, *Micromachines*, 2015, **6**, 216–229.
102 Y. Cong, S. Katipamula, T. Geng, S. A. Prost, K. Tang and R. T. Kelly, *Electrophoresis*, 2016, **37**, 455–462.
103 R. Zhong, M. Wang and B. Lin, *Electrophoresis*, 2023, **44**, 825–834.
104 A. Bußmann, T. Thalhofer, S. Hoffmann, L. Daum, N. Surendran, O. Hayden and M. Richter, *Micromachines*, 2021, **12**, 1459.
105 H. Sano, Y. Kazoe, R. Ohta, H. Shimizu, K. Morikawa and T. Kitamori, *Lab Chip*, 2023, **23**, 727–736.
106 Y. Wen, Y. Li, H. C. Chu, S. Cheng and Y. Zeng, *ACS Cent. Sci.*, 2024, **10**, 2059–2071.
107 Y. Wen, Y. Li, S. Cheng, J. Crow, G. Samuel, V. Vishwakarma and Y. Zeng, *ACS Nano*, 2025, **19**, 11973–11986.
108 A.-B. Siddique, J.-H. Weng, D.-K. Yang, C.-F. Chou and N. S. Swami, *Small*, 2025, **21**, 2412474.
109 D. Hümmer, F. Kurth, N. Naredi-Rainer and P. S. Dittrich, *Lab Chip*, 2016, **16**, 447–458.
110 Y. Wang, J. Zhu, P. Chen, L. Hu, X. Feng, W. Du and B. F. Liu, *Talanta*, 2019, **192**, 431–438.
111 A. P. Hsiao, K. D. Barbee and X. Huang, in *Proc.SPIE*, 2010, vol. 7759, p. 77590W.
112 J. Briones, W. Espulgar, S. Koyama, H. Takamatsu, E. Tamiya and M. Saito, *Sci. Rep.*, 2021, **11**, 12995.
113 K. K. Ho, L. M. Lee and A. P. Liu, *Sci. Rep.*, 2016, **6**, 32912.

114 V. Sanchez-Freire, A. D. Ebert, T. Kalisky, S. R. Quake and J. C. Wu, *Nat. Protoc.*, 2012, **7**, 829–838.
115 J. S. Marcus, W. F. Anderson and S. R. Quake, *Anal. Chem.*, 2006, **78**, 3084–3089.
116 B. J. Sanghavi, W. Varhue, A. Rohani, K.-T. Liao, L. A. L. Bazydlo, C.-F. Chou and N. S. Swami, *Lab Chip*, 2015, **15**, 4563–4570.
117 A. Rohani, B. J. Sanghavi, A. Salahi, K.-T. Liao, C.-F. Chou and N. S. Swami, *Nanoscale*, 2017, **9**, 12124–12131.
118 A. Rohani, W. Varhue, K.-T. Liao, C.-F. Chou and N. S. Swami, *Biomicrofluidics*, 2016, **10**, 033109.
119 J. Quist, S. J. Trietsch, P. Vulto and T. Hankemeier, *Lab Chip*, 2013, **13**, 4810–4815.
120 B. Sabbagh, E. Stolovicki, S. Park, D. A. Weitz and G. Yossifon, *Nano Lett.*, 2020, **20**, 8524–8533.
121 C. H. Chen, S. H. Cho, F. Tsai, A. Erten and Y. H. Lo, *Biomed. Microdevices*, 2009, **11**, 1223–1231.
122 Z. Cheng, X. Wu, J. Cheng and P. Liu, *Microfluid. Nanofluid.*, 2017, **21**, 1–11.
123 S. Sakuma, Y. Kasai, T. Hayakawa and F. Arai, *Lab Chip*, 2017, **17**, 2760–2767.
124 Y. Zhao, A. S. Abdelfattah, Y. Zhao, A. Ruangkittisakul, K. Ballanyi, R. E. Campbell and D. J. Harrison, *Integr. Biol.*, 2014, **6**, 714–725.
125 K. Cai, S. Mankar, T. Ajiri, K. Shirai and T. Yotoriyama, *Lab Chip*, 2021, **21**, 3112–3127.
126 R. Hulspas, L. Villa-Komaroff, E. Koksal, K. Etienne, P. Rogers, M. Tuttle and D. Berglund, *Cytotherapy*, 2014, **16**, 1384–1389.
127 T. H. Wu, Y. Chen, S. Y. Park, J. Hong, T. Teslaa, J. F. Zhong and P. Y. Chiou, *Lab Chip*, 2012, **12**, 1378–1383.
128 Y. Chen, T. H. Wu, Y. C. Kung, M. A. Teitell and P. Y. Chiou, *Analyst*, 2013, **138**, 7308–7315.
129 A. R. Abate, J. J. Agresti and D. A. Weitz, *Appl. Phys. Lett.*, 2010, **96**, 203509.
130 Y. Chen, Y. Tian, Z. Xu, X. Wang, S. Yu and L. Dong, *Appl. Phys. Lett.*, 2016, **109**, 143510.
131 S. H. Jin, B. Lee, J. S. Kim and C. S. Lee, *Chem. Eng. Sci.*, 2021, **245**, 116834.
132 Y. Gu, A. C. Zhang, Y. Han, J. Li, C. Chen and Y. H. Lo, *Cytometry, Part A*, 2019, **95**, 499–509.
133 K. Lee, S. E. Kim, S. Nam, J. Doh and W. K. Chung, *Micromachines*, 2022, **13**(12), 2105.
134 K. Zhang, Z. Xia, Y. Wang, L. Zheng, B. Li and J. Chu, *Lab Chip*, 2024, **24**, 4918–4929.
135 L. Gong, L. He, N. Lu, C. Petchakup, K. H. H. Li, C. Y. Tay and H. W. Hou, *Adv. Healthcare Mater.*, 2024, **13**, 2304529.
136 B. Y. Yu, C. Elbuken, C. Shen, J. P. Huissoon and C. L. Ren, *Sci. Rep.*, 2018, **8**, 3550.
137 M. Salek, N. Li, H. P. Chou, K. Saini, A. Jovic, K. B. Jacobs and M. Masaeli, *Commun. Biol.*, 2023, **6**, 971.
138 R. Tang, L. Xia, B. Gutierrez, I. Gagne, A. Munoz, K. Eribez and Y. H. Lo, *Biosens. Bioelectron.*, 2023, **220**, 114865.
139 X. Duan, X. Zheng, Z. Liu, T. Dong, Y. Luo, W. Yan and C. Song, *Anal. Chem.*, 2024, **96**, 1301–1309.
140 X. Chen, L. Waller, J. Chen, R. Tang, Z. Zhang, I. Gagne, B. Gutierrez, S. H. Cho, C.-Y. Tseng, I. Y. Lian and Y.-H. Lo, *APL Photonics*, 2021, **6**, 076101.
141 N. Nitta, T. Iino, A. Isozaki, M. Yamagishi, Y. Kitahama, S. Sakuma and K. Goda, *Nat. Commun.*, 2020, **11**, 3452.
142 N. Nitta, T. Sugimura, A. Isozaki, H. Mikami, K. Hiraki, S. Sakuma and K. Goda, *Cell*, 2018, **175**, 266–276.
143 M. Liu, P. Cataldi, R. J. Young, D. G. Papageorgiou and I. A. Kinloch, *Compos. Sci. Technol.*, 2021, **202**, 108592.
144 H. Xing, X. He, Y. Wang, X. Zhang, L. Li, Y. Wang and X. Li, *Mater. Today*, 2023, **68**, 84–95.
145 C. N. Nwosu, M. Iliut and A. Vijayaraghavan, *Nanoscale*, 2021, **13**, 9505–9540.
146 B. Song, E. Zhang, Y. Shi, H. Zhu, W. Wang, S. J. Gallagher and Z. Cao, *Langmuir*, 2025, **41**, 3464–3474.
147 A. J. Feliciano, E. Soares, A. W. Bosman, C. van Blitterswijk, L. Moroni, V. L. LaPointe and M. B. Baker, *ACS Biomater. Sci. Eng.*, 2023, **9**, 4619–4631.
148 R. H. Ali, V. Zammuto, M. Nicolò, F. De Leo, S. Lo Schiavo and C. Urzì, *Coatings*, 2025, **15**, 462.
149 X. Tang, S. Liang, Y. Jiang, C. Gao, Y. Huang, Y. Zhang and W. Wen, *Sci. Rep.*, 2021, **11**, 22162.
150 X. Kuang, S. Wu, Q. Ze, L. Yue, Y. Jin, S. M. Montgomery and R. Zhao, *Adv. Mater.*, 2021, **33**, 2102113.
151 F. Benito-Lopez, R. Byrne, A. M. Răduță, N. E. Vrana, G. McGuinness and D. Diamond, *Lab Chip*, 2010, **10**, 195–201.
152 M. R. A. Bhatti, A. Kernin, M. Tausif, H. Zhang, D. Papageorgiou, E. Bilotti and C. W. Bastiaansen, *Adv. Opt. Mater.*, 2022, **10**, 2102186.
153 B. Tavakol, M. Bozlar, C. Punckt, G. Froehlicher, H. A. Stone, I. A. Aksay and D. P. Holmes, *Soft Matter*, 2014, **10**, 4789–4794.
154 S. F. Ibrahim and G. van den Engh, in *Cell Separation: Fundamentals, Analytical and Preparative Methods*, ed. A. Kumar, I. Y. Galaev and B. Mattiasson, Springer Berlin Heidelberg, Berlin, Heidelberg, 2007, pp. 19–39.
155 S. Ramasamy, D. Bennet and S. Kim, *Int. J. Nanomed.*, 2014, **9**, 5789–5809.
156 S. Caixeiro, C. Kunstmann-Olsen, M. Schubert, J. Hill, I. R. Barnard, M. D. Simmons and M. C. Gather, *Adv. Opt. Mater.*, 2023, **11**, 2300530.
157 K. Eom, H. S. Park, D. S. Yoon and T. Kwon, *Phys. Rep.*, 2011, **503**, 115–163.
158 F. Chai and K. D. Kang, *Technologies*, 2021, **9**, 20.
159 J. Jarmoshti, A. B. Siddique, A. Rane, S. Mirhosseini, S. J. Adair, T. W. Bauer and N. S. Swami, *Small*, 2025, **21**, 2407212.
160 H. Lin and J. X. Cheng, *eLight*, 2023, **3**, 6.
161 S. López-Asunción and P. Ituero, *Electronics*, 2024, **13**, 1074.
162 G. Rutishauser, R. Hunziker, A. Di Mauro, S. Bian, L. Benini and M. Magno, in *2023 IEEE International Symposium on Circuits and Systems (ISCAS)*, 2023, pp. 1–5.
163 J. Riordon, M. Mirzaei and M. Godin, *Lab Chip*, 2012, **12**, 3016–3019.
164 S. B. Huang, Y. Zhao, D. Chen, H. C. Lee, Y. Luo, T. K. Chiu and M. H. Wu, *Sens. Actuators, B*, 2014, **190**, 928–936.
165 T. Julian, T. Tang, N. Tanga, Y. Yang, Y. Hosokawa and Y. Yalikun, *Lab Chip*, 2025, **25**, 5268–5282.
166 S. J. Sowerby, M. F. Broom and G. B. Petersen, *Sens. Actuators, B*, 2007, **123**, 325–330.

167 G. R. Willmott and L. H. Bauerfeind, *arXiv*, preprint, arXiv:1002, https://arxiv.org/abs/1002.0611.
168 R. Penchovsky, *Lab Chip*, 2013, **13**, 2370–2380.
169 J. Jarmoshti, A.-B. Siddique, P. Xu, A. Başlık, S. Mirhosseini, S. Mai, M. E. Kadin and N. S. Swami, *Biosens. Bioelectron.*, 2025, **289**, 117879.
170 G. Vishwanathan and G. Juarez, *Microfluid. Nanofluid.*, 2020, **24**, 69.
171 N. Willemstein, H. van der Kooij and A. Sadeghi, *arXiv*, preprint, arXiv:2503, https://arxiv.org/abs/2302.13141.
172 M. Vigogne, C. Zschech, M. Stommel, J. Thiele and I. Kühnert, *Macromol. Mater. Eng.*, 2024, **309**, 2400210.
173 M. S. Sotoudegan, O. Mohd, F. S. Ligler and G. M. Walker, *Lab Chip*, 2019, **19**, 3787–3795.
174 J. Ni, W. Xuan, Y. Li, J. Chen, W. Li, Z. Cao and J. Luo, *Microsyst. Nanoeng.*, 2023, **9**, 72.